Historical Ocean Subsurface Temperature Analysis with Error Estimates

MASAYOSHI ISHII

Climate Prediction Division, Japan Meteorological Agency, Tokyo, Japan

MASAHIDE KIMOTO

Center for Climate System Research, University of Tokyo, Tokyo, Japan

MISAKO KACHI

Earth Observation Research Center, National Space Development Agency of Japan, Tokyo, Japan

(Manuscript received 18 December 2001, in final form 19 June 2002)

ABSTRACT

An objective analysis of monthly ocean subsurface temperatures from 1950 to 1998 is carried out. The analysis scheme and the results with estimated analysis errors are presented.

The analysis domain is global with a horizontal grid of 1° × 1° and 14 vertical levels in the upper 500 m. Subsurface temperature observations used in the objective analysis are archived by the National Ocean Data Center of the National Oceanic and Atmospheric Administration, together with those collected through the global telecommunication system and domestic communication lines in Japan. All the observations are preprocessed by quality control and data selection procedures developed in this study. Together with these observations, three-dimensional fields of the upper-ocean temperature are optimally estimated using a variational technique. To ensure smooth and continuous vertical temperature profiles, a constraint term is introduced to the cost function that is minimized in the analysis. In addition, the analysis scheme is formulated to constrain mixed layer temperatures to become close to sea surface temperatures produced by the Met Office.

The three-dimensional structure of thermal anomalies is represented by the objective analysis. Interannual variations of temperature anomalies in the northern and tropical Pacific are presented and examined with the estimated errors. For the purpose of verification against independent observations of the objective analysis, dynamical heights estimated from the analyzed temperatures and climatological salinity are compared with tide gauge and sea surface height observations.

An investigation of analysis errors and signal-to-noise (S–N) ratio reveals that the reliability increases in the tropical Pacific since the 1970s and the S–N ratio for seasonally averaged temperatures in a 3° latitude × 6° longitude box at 100-m depth is 2.5 in the 1990s. This is not only due to the increase in data sampling but also to an increase in interannual variances of subsurface temperature. At midlatitudes of the Northern (Southern) Hemisphere, the S–N ratio is above (below) unity over the whole period of the objective analysis. The changes are very small in these 50 yr, although recent observational networks cover the global oceans better and the observations are more homogeneously distributed than those of the previous decades.

1. Introduction

The oceans are one of the most important elements in the global climate system, playing a dominant role on interannual, decadal, and longer timescales. In spite of their importance in climate studies, in situ oceanographic observations are not sufficient to represent fully the thermal and kinematic states of the oceans.

Sea surface temperature (SST) is the most precisely defined variable in time and space among oceanographical variables. The Met Office of the United Kingdom (UKMO) provides objectively analyzed SST fields for about 100 yr [Global Sea Ice and Sea Surface Temperature dataset (GISST); Parker et al. (1995)] based on historical ship observations archived in a dataset of UKMO and the Comprehensive Ocean and Atmosphere Data Set (COADS; Woodruff et al. 1987). However, sparseness of SST data is serious in the era prior to satellite observations and it is hard to interpolate SST data by ordinary statistical approaches. Owing to this difficulty, the grid data were first analyzed with conventional ship and buoy observations and reconstructed with the help of posterior knowledge, that is, using empirical orthogonal functions constructed from analyzed SSTs with ship, buoy, and satellite observations for a period of 1982–92 (Smith et al. 1996).

Corresponding author address: Masayoshi Ishii, Climate Prediction Division, Japan Meteorological Agency, 1-3-4, Otemachi, Chiyoda-ku, Tokyo 100-8122, Japan.
E-mail: ishii@naps.kishou.go.jp

Thanks to continuous efforts by many operational data centers, ocean observational data and hydrographic, chemical, and biological data have been collected and archived. One of the databases is compiled and distributed by the National Oceanographic Data Center (NODC) of the National Ocean and Atmosphere Administrations (NOAA; Levitus and Boyer 1994; Boyer and Levitus 1994). In addition, temperature and salinity climatologies have been produced by Levitus (1982), Levitus and Boyer (1994), and Levitus et al. (1994b). The latest climatology covers monthly variations at depths from sea surface to 1000 m.

Subsurface temperature analyses have been carried out with various approaches by several researchers (Smith 1995; White 1995; Levitus et al. 1994a). In this study, it is intended to combine optimally representative databases of SST and subsurface temperature: the GISST by UKMO and subsurface temperature observations by NOAA/NODC, to produce monthly subsurface temperatures. A new database is finally produced by objective analysis. It contains monthly ocean temperatures and analysis errors on a horizontal 1° × 1° grid at 14 levels in the upper 500 m during the period from 1950 to 1998. Before conducting the ocean temperature analysis, subsurface observations are categorized into suitable or unsuitable data for the objective analysis by quality control procedures described in section 2. An analysis scheme presented in section 3 is a maximum likelihood estimation, which is realized by a variational minimization. The scheme is formulated to produce smooth three-dimensional structures of sea water temperature with given surface and subsurface observations. In the objective analysis, a monthly climatology of oceanic temperatures given by Levitus and Boyer (1994) is used as the background temperature, or first guess. In section 4, the analyzed temperatures are presented together with estimated analysis errors, and the former is verified against sea level measured by tide gauges and sea surface height by the TOPEX/Poseidon satellite (Fu et al. 1994). Section 5 gives concluding remarks.

2. Data and quality control

Temperature observations in the upper 500-m depth are used for the objective analysis. These observations have to pass a seven-step check that is developed for the purpose of quality control and data selection as described below.

a. Data

Temperature observations used in the monthly analysis are from a database archived by NODC for the years between 1950 and 1990. For years 1991–98, another dataset is prepared, which merges two datasets: one archived by NOAA's Pacific Marine Environmental Laboratory (PMEL) and the other by the Japan Meteorological Agency (JMA). The PMEL dataset is a complete set of daily temperature observations by Tropical Ocean Global Atmosphere–Tropical Ocean Array (TOGA–TAO) buoys deployed in the tropical Pacific Ocean (Hayes et al. 1991; McPhaden 1995). The JMA dataset contains observations in the global oceans exchanged through the global telecommunication system and mostly in the seas around Japan transmitted by domestic communication lines in Japan.

Subsurface observations under the sea surface are distributed in the global oceans with a considerable inhomogeneity in their spatiotemporal density. Figure 1 depicts the geographical distribution of subsurface temperature profiles in each decade with the bottommost measurements at greater than 200-m depth. As shown in the figure, dense and frequent observations are seen in the Kuroshio and the Gulf Stream regions and along major routes of merchant ships. By contrast, few observations are available in the Southern Hemisphere during all the decades. Roughly speaking, observation frequency is one per month per 2° × 2° box in the Northern Hemisphere and one per season in the Southern Hemisphere for the whole period. Meanwhile, the homogeneity of the data distribution has been improved slightly in recent decades. Figure 2a shows the monthly number of observed temperature profiles from 1950 to 1998. About 5000 or more data profiles were reported in each month. Large seasonal fluctuations appear in their time series before 1975 owing to fewer observations in boreal winter than in boreal summer. The number of reported levels, that is, all levels in all the observational profiles, is also given in Fig. 2b, as indicated by the thin line.

Subsurface temperature profiles are stored in various formats with respect to vertical levels, for example, standard (interpolated) levels, actually measured levels, and every 1-dbar (about 1 m) level. Reports with sparse standard levels, for example, 0-, 50-, 100-, and 200-m depths, are very often seen in the databases. For easier handling of these observations, data interpolated to analysis levels could have been used in objective analysis rather than those with measured levels. However, the prior interpolation is avoided in this study, since the analysis described in section 3 is conducted in a three-dimensional space. By doing so, the characteristics in original temperature profiles can be preserved and interpolation errors are avoided for those profiles with sparsely reported levels.

Temperature climatology and its standard deviation are required both in the quality control and the objective analysis. In the quality control, the climatology is used as a reference for observation and the standard deviation gives empirical criteria for the quality control procedures. In the objective analysis, the climatology is used as the first guess; that is, departures from the climatology are calculated in the objective analysis. As described in section 3, the standard deviation is necessary to construct error covariance matrices of the first guess

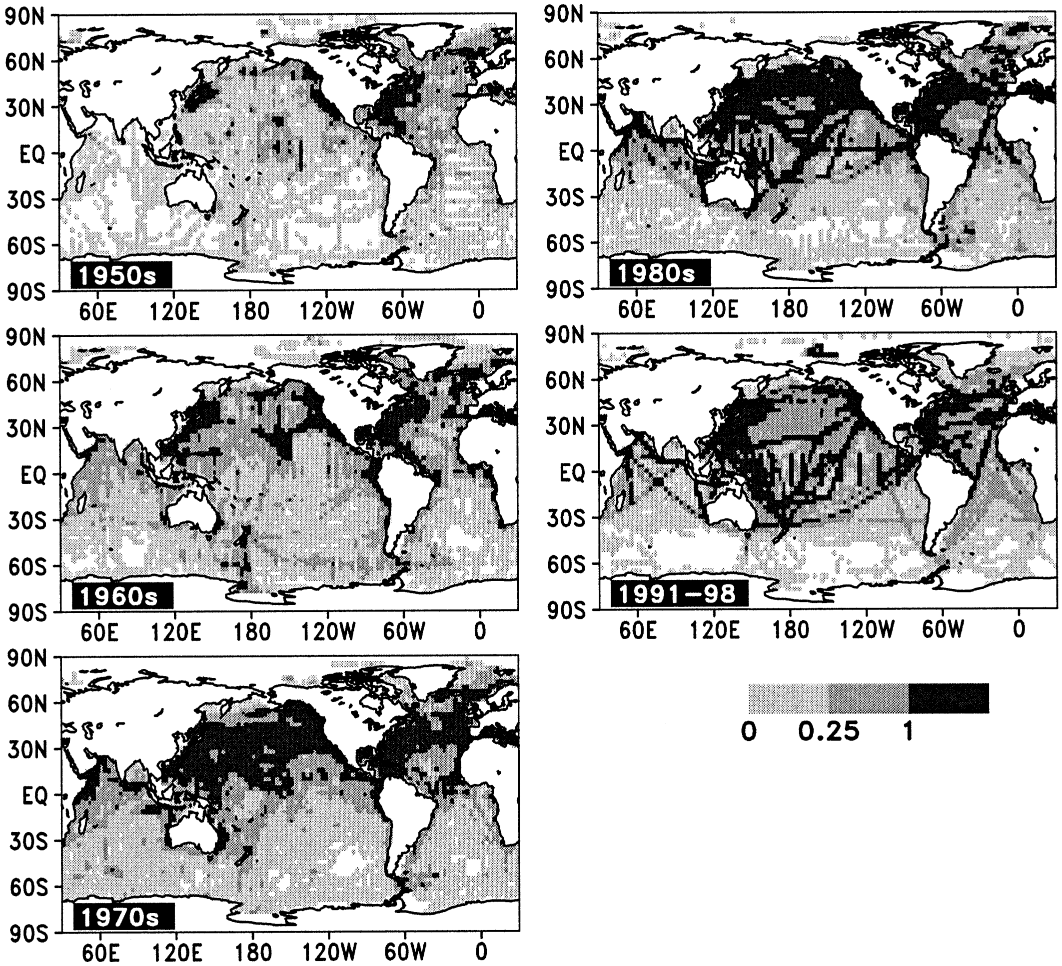

FIG. 1. Geographical distribution of subsurface temperature profiles whose bottommost measurements reach depths greater than 200 m for each decade. Shading indicates frequency of observation. Numbers 0.25 and 1 correspond to one observation per season and per month, respectively. Observations are counted in 2° × 2° lat–lon boxes. Blank areas represent no observations.

and of observations. Data suitable for the above purposes are provided by the *World Ocean Atlas 1994* (*WOA94*) compiled by Levitus and Boyer (1994), Boyer and Levitus (1994), and Levitus et al. (1994b). Their monthly temperature climatology is given on a 1° × 1° grid and 19 NODC standard levels in the upper 1000 m of the global oceans. The standard deviation of *WOA94* is however from 3-monthly mean statistics on a 5° × 5° grid. Hence, the standard deviation is linearly interpolated to a monthly 1° × 1° grid. The interpolated values may not represent well the spatiotemporal changes of the standard deviation on the finer grid. Nevertheless, this low accuracy has little importance in this study. The reasons are that the empirical criteria for the quality control procedures are given crudely, and that in the objective analysis, the error covariances are defined a priori and the ratio of the first guess error to the observational error is important rather than the magnitude itself.

Objective analysis of SST is not carried out in this study. Instead, monthly SST fields are defined by adding anomalies of the GISST data with respect to its own climatology defined for 1950–94 to the *WOA94* 0-m-depth climatology. The subsurface analysis utilizes this SST information in analyzing temperature in the mixed layer as described in section 3. The GISST dataset contains monthly analyzed SSTs and sea ice masks. The temperatures on the sea ice grid are set to -1.85°C. The sea ice information is also used for determining the existence of the mixed layer in the objective analysis (see section 3). However, the GISST does not cover the analysis period between 1995 and 1998. Therefore, it is replaced by an SST dataset analyzed by JMA using optimal interpolation (Nomura 1986) during this period. The JMA analysis uses satellite data retrieved by the National Environmental Satellite, Data, and Information Service (NESDIS) of NOAA. Root-mean-square differences between GISST and the JMA analysis are 0.4–1.0 in monthly and 5° resolution, which are comparable to those between GISST and an SST analysis by Reyn-

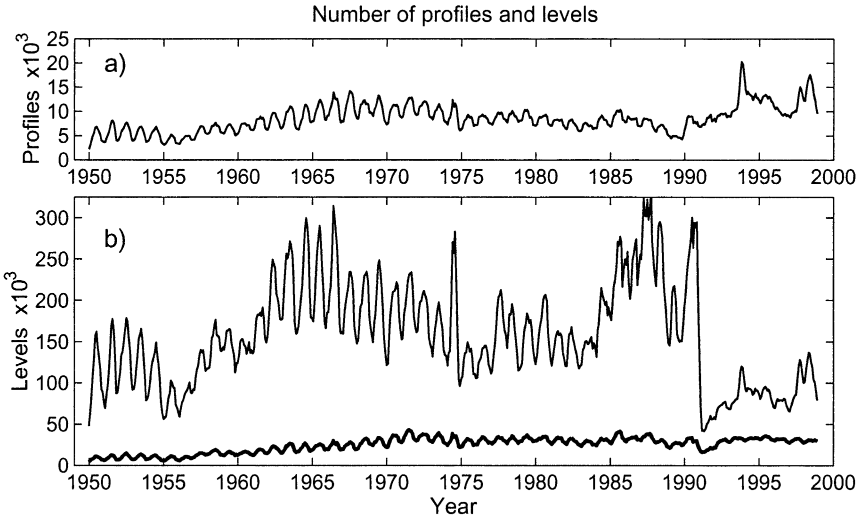

FIG. 2. Time series of monthly numbers of reported (a) temperature profiles and (b) levels. In (b), thin and thick lines indicate counts before and after the quality control and data reduction procedures, respectively. Vertical thinning and merging procedures mainly contribute to reduction of the counts. Refer to Table 1 and see text for details of the procedures.

olds (1988) at lower latitudes but slightly larger at high latitudes (refer to Fig. 3 of Folland et al. 1993).

b. Quality control and data reduction

Quality control procedures described below try to find erroneous data profiles. Furthermore, they also eliminate horizontal and vertical redundancy from the dataset. This redundancy originates from artificial aspects in an observation set, such as locally and temporarily dense observations and different reported vertical levels as pointed out in the above. As a consequence, the procedures reduce the volume of the dataset, and this lessens the computational costs required in the objective analysis. In order to eliminate horizontal redundancy, for instance, White (1995) introduced a concept called ‘‘super observations’’ to yield an observation set of seawater temperature randomly distributed in space and time (refer to appendix I of his paper for details). Similarly, but not taking the same approach as that of White (1995), the procedures ‘‘vertical thinning’’ and ‘‘merging’’ are introduced in this study, to reduce the vertical and horizontal redundancy, respectively.

In *WOA94,* erroneous observations are flagged by a quality control procedure that includes checks for (i) unusual temperature range, (ii) severe temperature inversion, (iii) depth inversion, (iv) duplication, (v) density inversion, and (vi) unrealistic features after an initial computation of the objective analysis (see *WOA94* for details). All the flagged observations are rejected from the database. Some of the expendable bathythermograph (XBT) profiles were corrected using an empirical formula for errors in XBT drop rates (Hanawa et al. 1995). A quality control procedure similar to that of *WOA94* is also performed on the PMEL and JMA merged dataset.

In the objective analysis, temperature observations available during a 120-day interval centered on the middle day of each calendar month are used. All the observations are inspected by a seven-step check, as shown schematically in Fig. 3. The following are the details of the check.

1) Location check: Observations at locations where the first guess values are not available, that is, on land, near coastal waters, or in canals, are rejected. Observations at depths greater than 500 m are not utilized except when temperatures at 500-m depth are linearly interpolated using 450–550-m depth observations.
2) Vertical thinning: Because of the use of reported level data, a procedure called vertical thinning is introduced to determine the minimum number of levels that preserve characteristics of the original data profiles. Sometimes the data profiles are given with densely measured levels. In this case also, the vertical redundancy is removed by this check. The procedure consists of the following two steps. First, temperature observations that are closest to the analysis levels and measured at the shallowest and the deepest depths are retained. Second, data not at the retained levels are inspected for rapid temperature changes between levels retained so far; a difference used for this check is calculated between a reported temperature and a linearly interpolated value using the adjacent two levels. If this difference exceeds a threshold 0.05°C, then the temperature is judged to change rapidly at the level and the observation is retained.

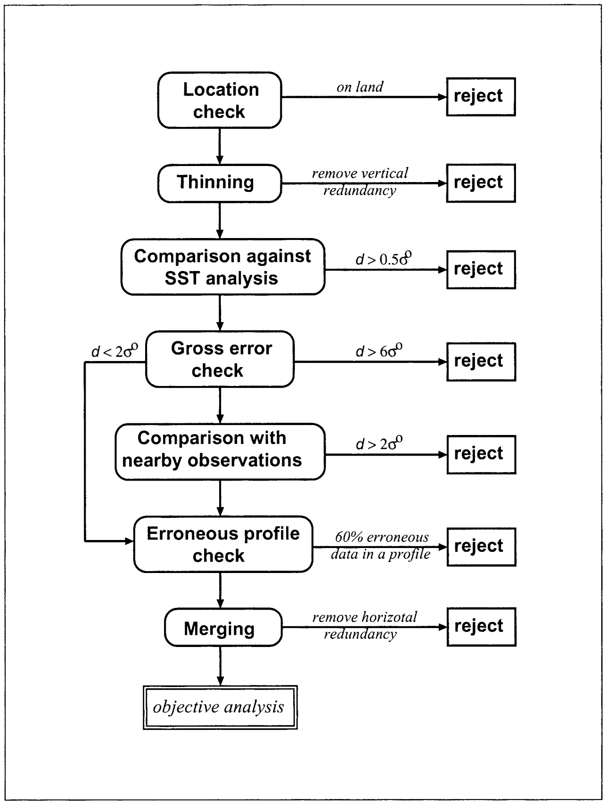

FIG. 3. The quality control and data reduction procedures adopted in this study. The letter d indicates the absolute departure from a reference used at each step, and σ^o is the standard deviation given by the *WOA94* dataset. All data are tested with the procedures except that the "comparison against SST analysis" check on data at high latitudes is bypassed. See text for further details of the procedures.

In subsequent steps, reference data are introduced and compared with individual temperature observations. There are three types of reference: climatology, analyzed SST, and an averaged temperature of observations spatially close to a datum in question. In the check, magnitudes of observational departure (d) from the reference are calculated first. Second, their magnitudes are assessed as to whether unrealistically large or not in comparison with the *WOA94* standard deviation (σ^o). The climatology, analyzed SST, and σ^o are given on the analysis grid and, hence, interpolated to both the date and the location of the observation in question.

3) Comparison against SST analysis: In this step, data are compared with the analyzed SSTs. The purpose is to avoid severe inversion within the mixed layer and to keep mixed layer temperatures close to the analyzed SST after the objective analysis. Thus, observations in and near the mixed layer are thoroughly inspected against the analyzed SSTs; if $d > 0.5\sigma^o$, the datum is rejected. This check however is bypassed for those measured at latitudes greater than 55°, where significant temperature inversion is common.
4) Gross error check: The check is to detect abnormal temperature observations compared with the *WOA94* climatology. Here, d indicates a departure from the climatology. If $d > 6\sigma^o$, the datum is rejected, while, if $d \leq 2\sigma^o$, the datum bypasses the next step (v).
5) Comparison with nearby observations: If $2\sigma^o < d \leq 6\sigma^o$ in the previous step, the datum is compared with nearby observations. Another reference value is calculated by weighted averaging the observations collected around the position of the datum under inspection. The collected data are from various ships and buoys but not from the one of the data points in question. The extent of this data collection is basically 4° × 4° in the horizontal and 20–200 m in the vertical. The horizontal extent is enlarged zonally in the Tropics, because, in the Tropics, the zonal coherence is larger than the meridional one, as discussed in section 3. In the vertical, the larger extent is used at the greater depth. The weight for the ith observation collected above is computed using a predetermined function of horizontal distance δr_i, vertical distance δz_i, and time lag δt_i between the ith observation and the observation in question:

$$w_i = \{(\sigma_i^o)^2 \alpha(\delta t_i)[1 + (\delta r_i/b)^2] \times [1 + (\delta z_i/c)^2]\}^{-1}, \tag{1}$$

where σ_i^o denotes the *WOA94* standard deviation interpolated to the ith position, the temporal correlation function α is given by a function of δt_i, and b and c are constant. Function α is constructed specifically for the monthly objective analysis. Rational functions are used as correlation functions representing horizontal and vertical coherency of temperature anomaly. In the correlation function for horizontal coherency, the decorrelation scale b, that is, the distance of the correlation coefficient 0.5, is set to 300 km, but δr_i is enlarged at lower latitudes taking the aspect ratio of the coherence of oceanic temperature anomalies into account. Further details of spatial and temporal correlation functions are given in section 3. The vertical decorrelation scale c is set to 50 m a priori, here. At this check, if the difference from the weighted average is within $2\sigma^o$, then the datum is retained for the subsequent analysis. In the case of an isolated observation, that is, no nearby observations are available for comparison, it is retained if $d < 3\sigma^o$.
6) Check for erroneous profiles: This procedure judges whether a temperature profile itself is reliable or not. If the number of flagged levels after all the above steps exceeds 60% in the profile, all the data of the profile are regarded to be erroneous and the whole profile is rejected.
7) Merging: As mentioned in section 2a, observation density differs greatly from one region to another. At this step, the horizontal and temporal redun-

TABLE 1. A result of the quality control for Jan 1987. A total of 1 053 343 levels in 27 571 profiles observed during 120 days from Nov 1986 to Mar 1987 are subjected to steps 1)–7) described in section 2b. Negative values indicate the number of rejected profiles or levels. After the seven-step check, observations at 124 733 levels are finally retained for the objective analysis.

	No. of levels
Total reported	1 053 343
Location	−244 422
Vertical thinning	−355 361
Against SST analysis	−33 800
Gross error	−322
Against nearby obs.	−26 239
Erroneous profile	−4142
Merging	−264 324
Retained	124 733

dancy is removed by a merging procedure. An ideal situation for the monthly objective analysis is that at least one observation exists at each grid point everyday. Thus, after steps (i)–(vi), all the neighboring observations within a lag of 1 day in a horizontal 1° × 1° box are merged into one. A value of the merged observation is calculated by averaging with weights given by Eq. (1).

An example of the result of the quality control procedures is given in Table 1. It contains the number of data profiles and reported levels, and negative values indicate the number of rejected profiles or levels during the check on observations in a 120-day interval from November 1986 to March 1987. After applying quality control procedures, the number of levels retained reduces to 1/10 of all the reported levels. One-third of all the reported levels are rejected by the vertical thinning and one-fourth by the merging. As shown in Fig. 2b, the monthly number of reported levels used in the objective analysis becomes more uniform in time after applying the quality control procedures (thick line) than before (thin line).

3. Analysis scheme

The monthly upper-ocean temperatures are objectively analyzed globally. The horizontal grid and depths of the vertical levels are the same as those of the *WOA94* climatology: 1° × 1° global grid and 14 layers placed at NODC standard depths of 0, 10, 20, 30, 50, 75, 100, 125, 150, 200, 250, 300, 400, and 500 m.

The analysis scheme adopted here is based on a variational minimization technique proposed by Derber and Rosati (1989) who applied it to ocean data assimilation. In this study, additional constraints are introduced to the analysis scheme. In addition, analysis errors are estimated. Temperature observations used in the objective analysis are collected from the 120-day window centered on day 15 of each calendar month. This size of the data window is adopted in order to collect at least one observation for each analysis grid on average (cf. Fig. 1). The first guess temperatures are given by the *WOA94* monthly climatology, and departures from the first guess are calculated in the objective analysis. Before conducting the objective analysis, we confirmed that an analysis result determined by a conventional optimum interpolation (OI) technique is similar to the one determined by the variational approach when the same data and the same analysis parameters are used in the two approaches.

a. Formulation

In the variational scheme, the following cost function is defined to be minimized:

$$J = \frac{1}{2}\mathbf{x}^{\mathrm{T}}\mathsf{E}^{-1}\mathbf{x} + \frac{1}{2}(\mathsf{D}\mathbf{x} - \mathbf{x}_o)^{\mathrm{T}}\mathsf{F}_1^{-1}(\mathsf{D}\mathbf{x} - \mathbf{x}_o) + \frac{1}{2}(\mathbf{x} - \mathsf{Q}\mathbf{x}_s)^{\mathrm{T}}\mathsf{F}_2^{-1}(\mathbf{x} - \mathsf{Q}\mathbf{x}_s) + \frac{1}{2}(\boldsymbol{\nabla}_z\mathbf{x})^{\mathrm{T}}\mathsf{G}^{-1}\boldsymbol{\nabla}_z\mathbf{x}. \quad (2)$$

In Eq. (2), vectors and matrices are denoted by lower- and uppercase, respectively. The superscript T indicates a matrix transpose. The vector $\mathbf{x}$ denotes three-dimensional temperature values to be obtained, and the scalar function J is minimized with respect to $\mathbf{x}$. The vertical differential operator $\boldsymbol{\nabla}_z$ is discretized by a centered finite difference and takes a matrix form in three-dimensional space. The cost function J is a sum of first guess and observational errors and two constraint terms, normalized, respectively, by the covariance matrices E for the first guess and $\mathsf{F}_i (i = 1, 2)$ for the observation and matrix G containing values of characteristic scales of vertical temperature gradients. The specification of E, F_i, and G is presented later. Observational data $\mathbf{x}_o$ are represented as deviations from the first guess linearly interpolated to the dates and the positions of $\mathbf{x}_o$ in three-dimensional space by a bilinear interpolation operator, D.

The first and second terms on the right-hand side of Eq. (2) act to optimize $\mathbf{x}$ considering error characteristics in the first guess and observational fields. If the cost function is formed only by the first two terms on the right-hand side, the scheme is equivalent to the one used by Derber and Rosati (1989).

The third term is to constrain mixed layer temperatures close to the analyzed SST, $\mathbf{x}_s$ (Kimoto et al. 1997). The mixed layer is defined as the uppermost layer where the temperature deviation from the SST is within 0.5°C. The depth of the layer is called the mixed layer depth (MLD) and denoted by h. The matrix Q in the third term contains error covariances with respect to mixed layer temperatures. In fact, the components of Q represent the three-dimensional distribution of the first guess mixed layer and weight decreasing with the depth ($z < h$) as $1 - 0.9 (h - z)/h$. In this study, a constant reduction rate of the weight, 0.9, is assumed. If the sea

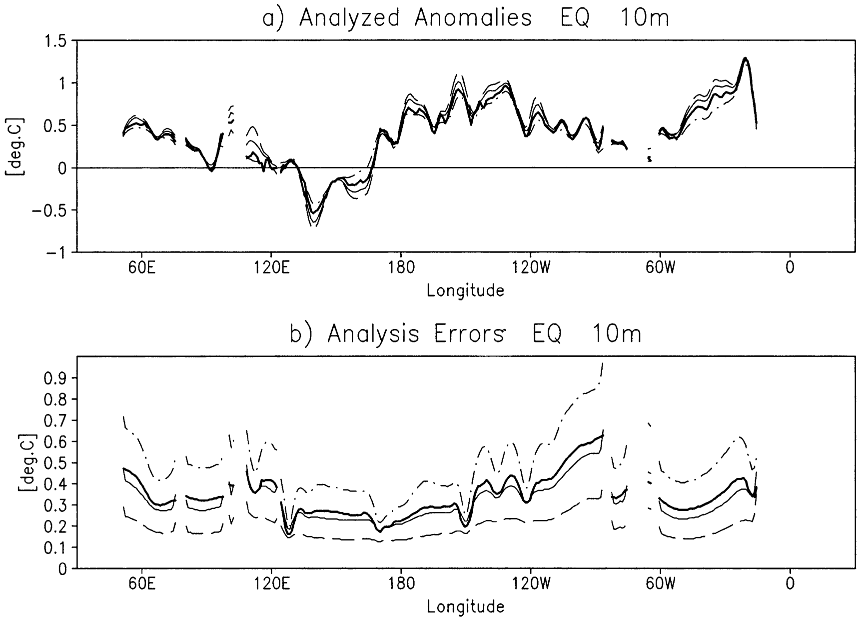

FIG. 4. Comparison among tests with and without nondiagonal components of $\mathbf{F}_2$. (a) Analyzed anomalies (°C) at 10-m depth along the equator and (b) the corresponding analysis errors (°C). The thick solid lines indicate a result of the test with the nondiagonal components, where the error variance of the analyzed SST is set to $0.5(\sigma_o)^2$. Among tests without the nondiagonal components, the error variance is set to $(0.7\sigma_o)^2$, $(\sigma_o)^2$, or $(1.5\sigma_o)^2$.

surface is completely covered with sea ice, MLD is set to zero. This is done because deep convection is not expected unlike in open oceans. In addition, convection due to the extrusion of salt from sea ice is not considered. Thus, the matrix $\mathbf{Q}$ is diagonal and proportional to $\mathbf{F}_1$ defined below. Although the horizontal correlation of the analyzed SSTs should be considered in $\mathbf{F}_2$, the nondiagonal components are ignored in this study for simplicity. Instead, large variances are given to the diagonal components of $\mathbf{F}_2$, considering the effective number of observations. To make this simplification valid, tests with and without nondiagonal components of $\mathbf{F}_2$ are undertaken. Here, the error variance of the SST analyses is assumed to be half of the observational error variance, $(\sigma_o)^2/2$. Figures 4a and 4b show analyzed anomalies at 10-m depth along the equator and the corresponding analysis errors estimated using an optimal interpolation technique. Among the tests without the nondiagonal components, the error variance of the analyzed SST is set to $(0.7\sigma_o)^2$, $(\sigma_o)^2$, or $(1.5\sigma_o)^2$, and the results are shown with broken, thin solid, and dashed–dotted lines, respectively. Thick solid lines indicate results from the test with diagonal components. The analyzed anomalies appear to be insensitive to both the sizes of the error variance and the presence of the nondiagonal components in $\mathbf{F}_2$, and the differences are mostly within the analysis errors. On the contrary, the analysis errors do not behave likewise. In the case of $(\sigma_o)^2$, the analysis errors are nearly equal to those of the test with nondiagonal components. Therefore, this variance is used to construct matrix $\mathbf{F}_2$ without the nondiagonal components in the present analysis.

The fourth term is the so-called Tikhonov's term, which is a technical device for regularization of ill-posed inverse problems (refer to Golub et al. 2000 and their bibliography). The main purpose of this term is to substitute for that vertical decorrelation of the first guess error covariances, which is ignored to reduce computational costs. This term ensures vertical smoothness in analyzed profiles. The matrix $\mathbf{G}$ is diagonal. The components of $\mathbf{G}$ denote the strength of the vertical smoothing and are assumed to be larger in the mixed layer than outside by a maximum factor of 3 near sea surface, in order to prevent a large temperature inversion in the mixed layer.

To avoid direct calculation of J that involves inversion of the big matrix $\mathbf{E}$, a preconditioned conjugate gradient algorithm (Gill et al. 1981; Derber and Rosati 1989) is adopted. The algorithm improves $\mathbf{x}$ by an iterative calculation. In the most cases, changes of $\mathbf{x}$ between iterations become substantially small after 15 iterations. Therefore, the number of iteration is fixed in this study to a constant 20.

b. Error covariances

As mentioned briefly in section 2, a rational function is adopted in this study in order to represent the spatial coherency of the temperature anomaly. Julian and Thiebaux (1975) present various types of correlation functions together with these analytic forms of the Fourier transformation. As listed in Table 1 of Julian and Thiebaux (1975) rational functions are used as a function for damping as well as exponential functions. The correlation functions they proposed also include cosine and Bessel functions to represent periodic features seen in sample data, but these are usually ignored in recent studies. Rational functions are sometimes preferable because of practical reasons: better fitting to sample data and lower computational cost than those of exponential functions.

The first guess error covariance matrix $\mathbf{E}$ is represented by a predefined rational function of geographical distance r_{ij} between grid points i and j:

$$E_{ij} = \frac{\sigma_i^o \sigma_j^o}{1 + (r_{ij}/b)^2}. \qquad (3)$$

The magnitude of the first guess error variance at grid point i, E_{ii}, is identical to that of *WOA94,* $(\sigma_i^o)^2$, because departures from the climatology are analyzed in this study. In addition, the equation ensures the symmetricity of $\mathbf{E}$ and represents geographical change in first guess error variances. According to White (1995), a horizontal decorrelation scale of the first-guess temperature, b, varies with depth, but the constant value, 300 km is used here for simplicity. An elliptic structure is assumed for the horizontal shapes of covariance $\mathbf{E}$ at latitudes lower than 60°: larger zonal coherence than meridional coherence (Bottomley et al. 1990; Sprintall and Meyers 1991). To realize this, the distance r_{ij} between grid points i and j is computed with an ''enlarged'' longitudinal distance by a factor of $3\,(1 - |\theta|/90)$, where θ is the central latitude between the two grid points. Because of the use of the *WOA94* standard deviation, the error variance of the first guess changes geographically and seasonally. Moreover, it is ensured that covariances for pairs of grid points in different ocean basins are equal to zero.

Although the covariance matrix $\mathbf{E}$ does not include vertical decorrelation, multiplying a vector by $\mathbf{E}$ is still a costly operation. Therefore, covariances of the first guess are calculated on a coarse grid. The coarse grid spacing used here is twice that of the original grid. In this case, the computational load for the calculation of the covariances reduces to 1/16th, since it is proportional to the square of the number of horizontal grid points.

Let $\mathbf{P}$ be a linear interpolation operator that maps a variable $\mathbf{y}$ on the coarse grid to a variable $\mathbf{x}$ on the original grid, $\mathbf{x} = \mathbf{P}\mathbf{y}$. By the definition of covariance, a covariance matrix $\hat{\mathbf{E}}$ for $\mathbf{x}$ is computed from a covariance matrix $\mathbf{E}'$ for $\mathbf{y}$ as

$$\hat{\mathbf{E}} = \mathbf{P}\mathbf{E}'\mathbf{P}^t. \qquad (4)$$

The covariance matrix $\mathbf{E}'$ on the coarse grid is defined as in the case of $\mathbf{E}$. The reconstructed covariances of $\hat{\mathbf{E}}$ near zero distance are generally smaller than those of $\mathbf{E}$, because variances on small horizontal scale represented on the fine grid are filtered out on the coarse grid. By direct calculation, it is found that the trace of $\hat{\mathbf{E}}$, namely the total error variance of the first guess, reduces to about 70% of $\mathbf{E}$. In fact, the reduction amount depends on the selection of the coarse grid, the interpolation method, and the spatial structure of the error covariance. In the objective analysis, the analysis result is affected by this reduction. In the case of $\hat{\mathbf{E}}$, the ratio of observational error to first guess error becomes smaller than that in the case of $\mathbf{E}$. For this reason, an analyzed temperature field with $\hat{\mathbf{E}}$, becomes smoother than that with $\mathbf{E}$. In other words, $\hat{\mathbf{E}}$ works as an enhanced low-pass filter in the horizontal space. No more significant differences appear in the above analyzed field with $\hat{\mathbf{E}}$. Since there is no truly rigorous guidance in estimating the ratio between the magnitudes of observation and first guess errors and hence in determining the optimal smoothness in the analyzed fields, we made no adjustment to the slight underestimation by use of $\hat{\mathbf{E}}$ in place of $\mathbf{E}$.

In the observational error covariance matrix $\mathbf{F}_1$, no correlation among different observations is assumed. Hence, the matrix $\mathbf{F}_1$ is given by a diagonal matrix,

$$F_{1,kl} = \sigma_k^o \sigma_l^o \delta_{kl} w_k \alpha(\delta t_k), \qquad (5)$$

where the variables are the ones used in Eq. (1) except for the Kroneker's delta, δ_{kl}, a weight for the kth observation, w_k, and time lag in days between dates of the observation and the analysis, δt_k. It is better to change the weight w_k according to individual observation types, for example, ship, buoy (cf. Reynolds and Smith 1994), but w_k is set constant in this study because no reliable statistics are available at present.

When short-term (e.g., 1–10 days) temperature fields are analyzed with an adequate number of data in a small data window, the temporal decorrelation is set to unity for all time lags as in Reynolds and Smith (1994). This can be done because the temporal decorrelation scale of oceanic temperature anomalies is comparatively long. For instance, a decorrelation scale of about 2 weeks is obtained by Nomura (1986) using a set of SST observations. However, a reasonable decorrelation α in Eq. (5) is to be defined for a much larger data window. In this study, a methodology is adopted to construct temporal decorrelation for the monthly objective analysis. In general, the monthly mean values are obtained by arithmetic averaging of daily analyses. Similarly, temporal decorrelation coefficients used for the monthly objective analysis are defined as the sum of the ones for daily analysis normalized by the maximum value centered in the data window. The decorrelation coefficients for the daily analyses are given by a function, $1/(1 + \delta t_k/15)$, where the decorrelation scale of 15 days is set following the reliable statistics with SST observations. In fact, the temporal decorrelation scale varies in depth (White 1995), but it is assumed constant for simplicity.

The error variance of the kth merged observation (section 2) is redefined as $(\sigma_k^o)^2(n + 1.8n_s)/n^2$, where n is the number of data points used for the combining, and n_s by the same ship/buoy among n observations. A large correlation coefficient, 0.9, which is half of 1.8, is assumed among n_s observations, since the observations are temporally and spatially close to each other.

c. *Estimate of analysis errors*

In order to provide a measure of the quality of products, analysis errors are estimated. When the third and fourth terms on the right-hand side of Eq. (2) are omitted, a covariance matrix for the analysis errors is written as $(\mathbf{I} - \mathbf{KD})\mathbf{E}$, where $\mathbf{K} = \mathbf{ED}^t(\mathbf{DED}^t + \mathbf{F}_1)^{-1}$ and $\mathbf{I}$ is the identity matrix. Refer to Ghil and Malanotte-Rizzoli (1991) for further details on the derivation of the analysis error covariance. The expression includes matrix–matrix multiplications; therefore, a huge amount of computation is required to obtain even the diagonal components of the analysis error matrix. For this reason, the analysis errors are evaluated using an optimal interpolation technique in which the covariance matrix is constructed, respectively, at each grid point by observations locally distributed around the grid point.

An error for the analyzed temperature averaged in time and space is also defined using the analysis errors obtained above. In general, error variance is reduced by temporal and spatial averaging over sampling data. On the basis of this rule, the error for the averaged temperature is estimated as an area average of the analysis errors with weights that are spatiotemporal decorrelation coefficients for the analyzed temperature anomalies. In the above estimation, the spatial and temporal decorrelation scales are 40% of those used in the objective analysis. These decorrelation scales are estimated from temperature differences between observed and analyzed temperatures for 1971–90. The result seems to be reasonable because analyzed temperatures include variances of observation and because it is not necessary to consider any other systematic errors in the present analysis. When temporal decorrelation coefficients at lags greater than 60 days are required later for the estimation of analysis errors, the coefficients are computed by the same manner as that in the objective analysis.

4. Analysis results and verification

Monthly fields of analyzed subsurface temperature and associated analysis errors during 1950–98 are produced by the method described in the previous section. In this section, interannual changes in oceanic temperatures are presented first. Second, the historical changes in the analysis errors are discussed in terms of signal-to-noise (S–N) ratio, which evaluates the reliability of the analysis outputs. Another S–N ratio is computed to compare the present analysis with dynamic–statistical analyses, that is, so-called data assimilation. Finally, dynamic heights computed using analyzed temperature and climatological salinity are compared at latitudes between 60°S and 60°N with sea level observations from tide gauges and sea surface heights measured by the TOPEX/Poseidon satellite, both of which are independent of the temperature analysis.

As a first example of the objective analysis, thermal fields for January 1987, in the midst of an El Niño, are presented in Fig. 5. In the left-hand-side column, analyzed temperatures are plotted in a longitude–latitude section at 125-m depth (Fig. 5a), a latitude–depth section along 165°E (Fig. 5c), and a longitude–depth section along the equator (Fig. 5e). The corresponding analyzed deviations from the *WOA94* climatology, namely anomalies, are shown in Figs. 5b, 5d, and 5f, respectively. In these panels, light and thick shadings indicate analysis errors larger than 1°C and less than 0.5°C, respectively. In this month, large temperature anomalies appear in the tropical Pacific Ocean: negative anomalies less than −1°C on the western side and positive ones greater than +1°C on the eastern side. These anomalies are related to the 1986–87 El Niño (e.g., Miller et al. 1988). According to the *WOA94* climatology, in January, MLDs along 165°E reach more than 100 m north of 40°N and south of 70°S, and are shallower than 50 m between 10° and 70°S. Owing to the use of the analyzed SSTs to make these analyses of the mixed layer temperatures, large deviations appear near the sea surface even at high latitudes.

In this study, the first guess errors are equivalent to the standard deviation of *WOA94*, σ^o. Thus, analysis errors become smaller than σ^o anywhere, but they also become very close to σ^o when few observations are available. Whereas the first guess errors are more than 0.5°C mainly in all the regions in the sections presented in Fig. 5, the analysis errors are smaller than 0.5°C near the sea surface and in deep layers. Along the thermocline and in the Kuroshio area and its extension regions, the first guess errors exceed 1.5°C, but the analysis errors less than 1°C are seen in part there. Roughly speaking, the analysis errors are reduced by more than 40% of σ^o along the major sea routes (refer to Fig. 1) and in MLDs, and by at most 5% in data-sparse regions.

The analysis errors calculated with the theoretical formulas (section 3) are validated using TAO buoy observations for the period 1990–98. Figure 6 shows profiles of analysis errors (thick solid) and root-mean-square differences (rmsd's, thick broken) between analyzed temperatures and equatorial TAO buoy observations at 165°E, 140°W, and 110°W. An additional analysis, from which the TAO data are withheld, is performed in order to see the uncertainty in estimating subsurface temperatures and the sensitivity of observations to the analysis errors. The result is shown with corresponding thin lines. Decrements due to the use of TAO data are consistently seen in the analysis errors and the rmsd's. Noting that the rmsd's include observational errors, the errors estimated theoretically do not differ much from the rmsd's. The analysis errors are much larger than the decrements, and at depths below 200 m, the errors are

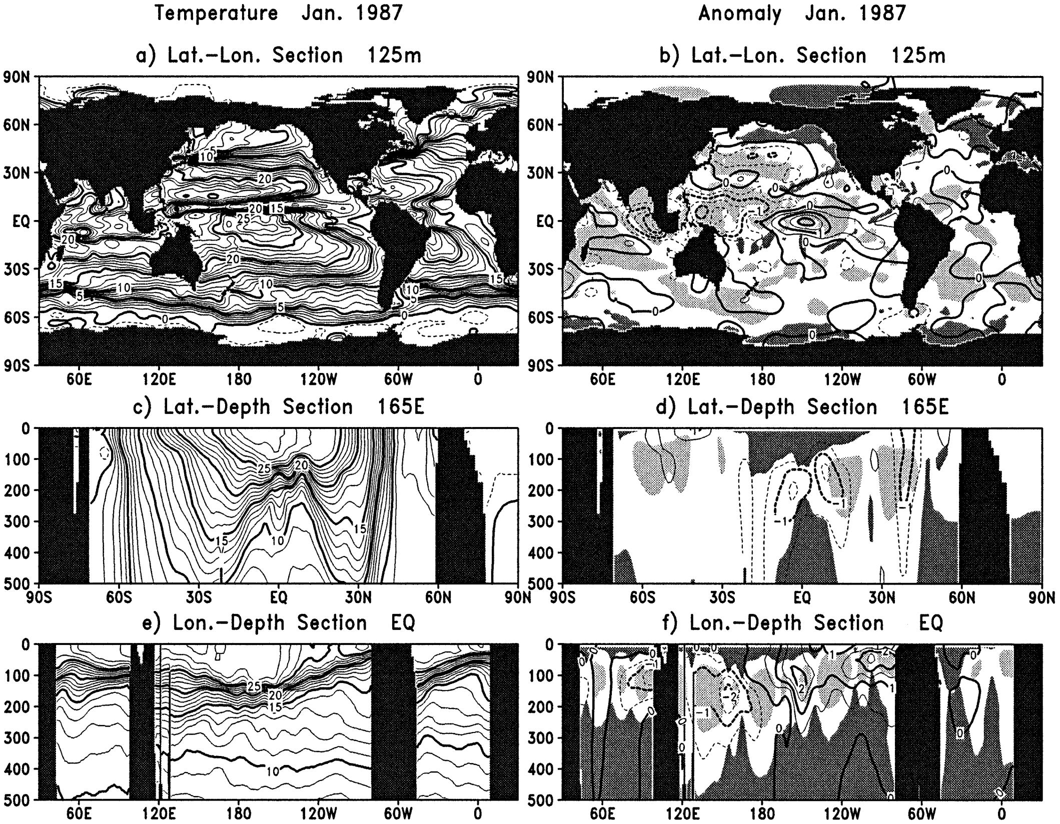

FIG. 5. (left) Analyzed temperatures and (right) the deviations from the *WOA94* climatology for Jan 1987. Lat–lon sections (a), (b) at 125-m depth, (c), (d) latitude–depth sections along 165°E, and (e), (f) longitude–depth sections along the equator. A contour plot of analyzed temperatures is shown in the left-hand-side column. Contour interval is 1°C with broken lines indicating negative temperatures. At the sea ice grid, temperatures are set to −1.85°C. In (b), (d), and (f), deviations from the *WOA94* climatology and analysis errors are shown with contours and shadings, respectively. Contour interval is 0.5°C and solid and dashed contours stand for positive and negative deviations, respectively. The light and thick shading indicates analysis errors greater than 1°C and less than 0.5°C, respectively.

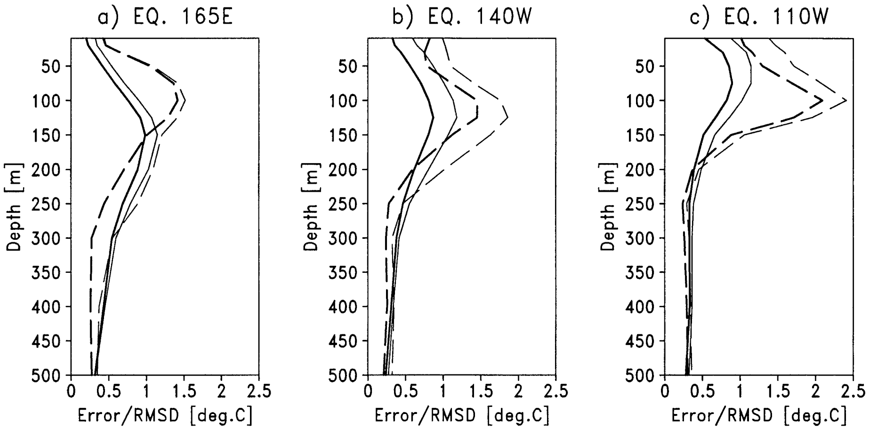

FIG. 6. Analysis errors (thick solid line) and rmsds (thick broken line) between the analyses and equatorial TAO buoy observations at 165°E, 140°W, and 110°W. Corresponding thin lines indicate a result obtained from an objective analysis from which the TAO data are withheld. The period of statistics is 1991–98.

comparable to rmsds for the analysis done withholding the TAO data (thin broken line). This implies that the estimated errors are appropriate as a measure of uncertainty. There are some discrepancies between the standard deviations of TAO buoy data and *WOA94*. These cause portions of differences between the analysis errors and the rmsd particularly at thermocline depths.

In the following subsections, temperature anomalies are computed as departures from averages of the analyzed data for the period 1961–90 as long as they are not specified otherwise.

a. Interannual variations of oceanic temperature

Interannual variations of thermal structures in the tropical and North Pacific are presented in this section.

Figure 7 shows time series of temperature anomalies along the thermocline in the tropical Pacific with a function of longitude at the equator and 10°N. Here, the 20°C isothermal depth is used as a proxy to indicate the thermocline (cf. Fig. 5). Roughly speaking, the temperature anomaly of 1°C corresponds to a depth anomaly 10 m. Along the equator (Fig. 7a), areas of positive and negative anomalies with magnitudes greater than 1°C alternately propagate eastward in the Pacific basin, associated with El Niño and La Niña events, respectively. The peak values of temperature anomalies are clearly seen after the 1980s, reflecting highly frequent observations by TOGA–TAO buoys. The largest positive anomalies appear in the years 1982–83 and 1997–98 as a result of strong coupling between the ocean and the atmosphere (Gill and Rasmusson 1983; Webster and Palmer 1997; McPhaden 1999; Wang and Weisberg 2000). The peak positive anomalies for 1986–87 and 1991–92 are large as well. Before the 1980s, several El Niño events are recognizable in the figure as the ones documented by Busalacchi and O'Brien (1981), Rasmusson and Carpenter (1982), and Busalacchi et al. (1983). At 10°N (Fig. 7b), temperature anomalies propagate westward, and the magnitudes of the anomalies are smaller than those at the equator.

In Fig. 7a, the amplitudes of the positive temperature anomaly during the 1986–87 and 1991–92 events are comparable to that in the 1982–83 event. The corresponding SST anomalies during the first two events, however, were not so large (see, e.g., Fig. 4 of McPhaden 1999). By contrast, the amplitude of the positive anomaly propagating westward is largely seen for seasons following the 1983–84 event in the right-hand-side panel. In the 1982–83 case, observations seem to be insufficient to reproduce faithfully the temperature anomalies below the sea surface. In fact, the analysis errors in the eastern Pacific temporarily become large from November 1982 to January 1983. Moreover, during the mature phase of the event, subsurface temperature observations used in the analysis are limited for longitudes from 150° to 120°W, near the equator.

Figure 8 displays interannual variations of temperature anomalies at 150-m depth in the western Pacific. The analysis errors (shaded) are overlaid on 12-month running averages (thick line) of monthly temperature anomalies (thin line). Here, the temperature anomalies are spatially averaged over 1°S–1°N and 135°–165°E, and the corresponding analysis errors are calculated in the manner described in section 3. No smoothing is applied on the monthly anomalies. The amplitude of the anomalies becomes larger in recent decades than before, and the monthly anomalies are less than −2°C during major El Niño events occurring in the 1980s and the 1990s. Before the mid-1960s, the magnitude of the temperature anomalies is mostly smaller than that of the analysis errors. On the other hand, significant negative and positive anomalies greater than the analysis errors appear after the mid-1960s associated with El Niño and La Niña, respectively. While the amplitude of the anomalies becomes large, the analysis error becomes small: about 0.7°C before the mid-1960s, about 0.5°C from the mid-1960s to the mid-1980s, and about 0.4°C or less after the mid-1980s.

In Fig. 7a, positive temperatures are dominantly seen from the late 1960s to the 1970s west of the date line at the equator, and an opposite tendency is seen after the 1980s. Here, we examine whether this decadal change is significant or not using the time series shown in Fig. 8. This time series is almost the same as the one averaged from 135° to 165°E in Fig. 7a. Ten-year mean temperature anomalies for 1967–76 and 1982–91 are 0.79° and −0.73°C, respectively, while the corresponding analysis errors are estimated as 0.36° and 0.31°C, respectively. The two 10-yr periods are selected because positive and negative anomalies are dominantly seen, respectively, in Fig. 8. Consequently, the decadal change is regarded as statistically significant at the 95% confidence level. This is an example of error analysis and more detailed discussions on the interdecadal change are beyond the scope of this paper.

Temperature anomalies and MLDs averaged over 30°–45°N, 150°–170°W are presented in Fig. 9. The values are plotted as a function of depth from sea surface to 375 m. A significant interdecadal change is seen in the temperature anomalies; positive temperature anomalies (thick shading) are dominant in the 1960s, and the negative anomalies (light shading) are dominant in the 1980s. The transition occurs around the mid-1970s. Such an interannual change is also found in the upper oceans as pointed out by Deser et al. (1996) with temperature anomalies at selected levels of every 100 m from the sea surface to 400-m depth over the same regions as that in Fig. 9. The magnitude of the analysis error of yearly averaged temperatures over this region at 100-m depth is within a range, 0.2°–0.35°C, during the period. The historical changes in analysis error are discussed later. In the vertical, the analysis errors become small by about 0.04°C $(100\ \mathrm{m})^{-1}$.

The significance of the interdecadal change before and after the mid-1970s in Fig. 9 is tested here, as is

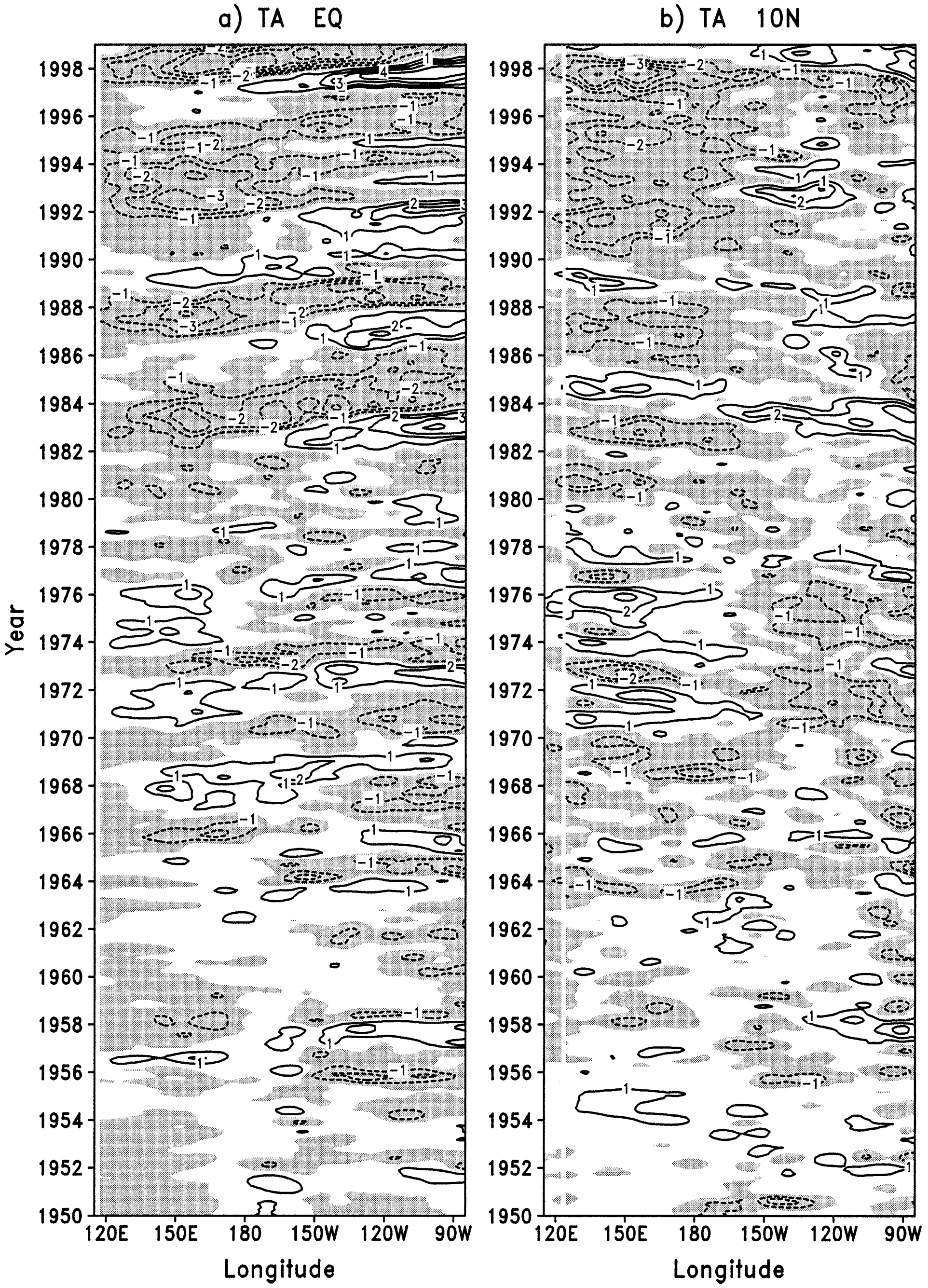

FIG. 7. Time series of temperature anomalies (°C) at thermocline depths defined by the 20°C isotherm along (a) the equator and (b) 10°N in the Pacific Ocean for 1950–98. Contour interval is 1°C and negative values are shaded. Five-month running averaging is applied to time series at all the longitudes.

done for the case of the interdecadal change that occurred in the equatorial western Pacific. At 100-m depth, the averaged temperature anomalies for 1967–76 and 1977–86 are 0.24° and −0.33°C, respectively, and the corresponding analysis errors are estimated to be 0.18° and 0.16°C, respectively. Therefore, the change can be regarded as significant at the 95% confidence level. Tests at 50- and 200-m depths result in significant changes at the 90% confidence level, that is, larger than the error standard deviation, but a marginal change at 300-m depth.

In the monthly climatological temperature fields, MLDs in this area reach the maximum depth of 140 m in February and become the shallowest, at about 15 m, in July. The MLDs also fluctuate over the decades especially from winter to early spring. The amplitude of

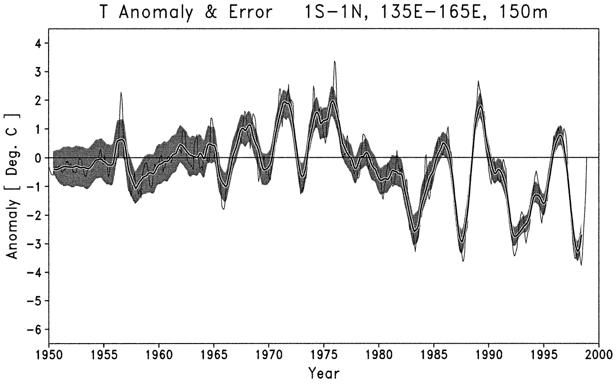

FIG. 8. Time series of temperature anomalies (°C) and the analysis errors (°C) averaged at 1°S–1°N, 162°–168°E at the depth of 150 m for 1950–98. The thin and thick lines indicate monthly temperature anomalies and their 12-month running averages, respectively. The analysis errors are represented by shading on the upper and lower sides of the thick line.

the interannual variability exceeds 30 m from February to April when the MLDs become shallow. As shown in Fig. 9, positive (thick shading) and negative (light shading) temperature anomalies are generated in wintertime associated with the deepest MLD (thick line). Once the thermal anomalies are excited, the anomalies persist below MLD throughout the year and extend deeper. This process is known as subduction (e.g., Schneider et al. 1999). However such a process is hardly seen in the 1950s probably owing to data sparseness.

Concerning the transition phase of upper-ocean temperatures in the mid-1970s displayed in Fig. 9, temperature anomalies for 7 yr are shown as latitude–depth sections along 157.5°W and 177.5°E in Fig. 10. The figure format follows that of Fig. 2 of Zhang et al. (1998). As discussed by Zhang et al., for yearly 5° × 5° analysis data (Zhang and Levitus 1996), positive anomalies are formed in MLDs at latitudes from 30° to 40°N and then they move downward and travel southward along isopycnal surfaces indicated by thin, solid lines for every 1 kg m^{-3}. There are however several subtle differences in Fig. 10 from Zhang et al.'s; the magnitudes of the anomalies are slightly larger than theirs, and local peaks separately appear in the map: for instance, two local peaks of positive anomalies located at depths of 100–300 m from 10° to 25°N in Fig. 10c. Furthermore, the anomalies generated in the central North Pacific split in two and move down and southward individually in their subduction processes. These discrepancies appear to be caused by differences in the analysis method and the spatiotemporal resolution between the two datasets. In addition, according to our

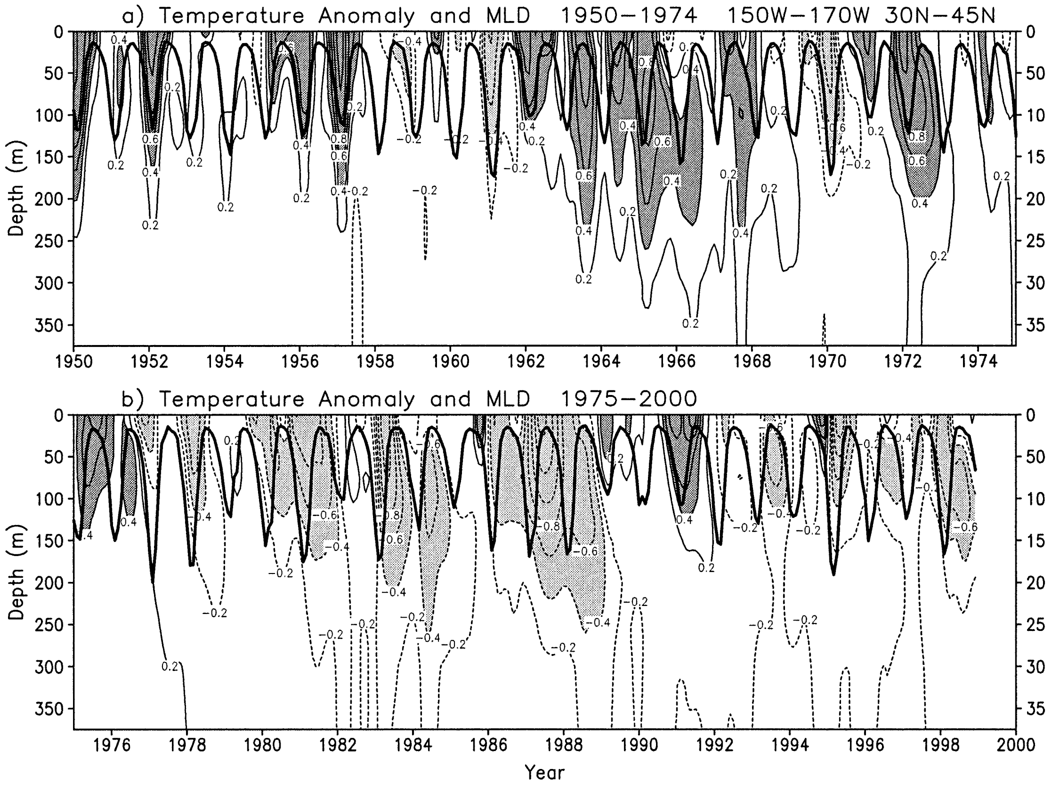

FIG. 9. Time–depth section for averaged temperature anomalies (thin solid and dotted lines) and mixed layer depths (thick lines) averaged at 30°–45°N, 150°–170°W, for the periods (a) 1950–74 and (b) 1975–98. Contour interval for temperature anomalies is 0.2°C and zero contours are omitted. Thick and light shadings indicate positive temperature anomalies greater than 0.4°C and the negatives less than −0.4°C, respectively.

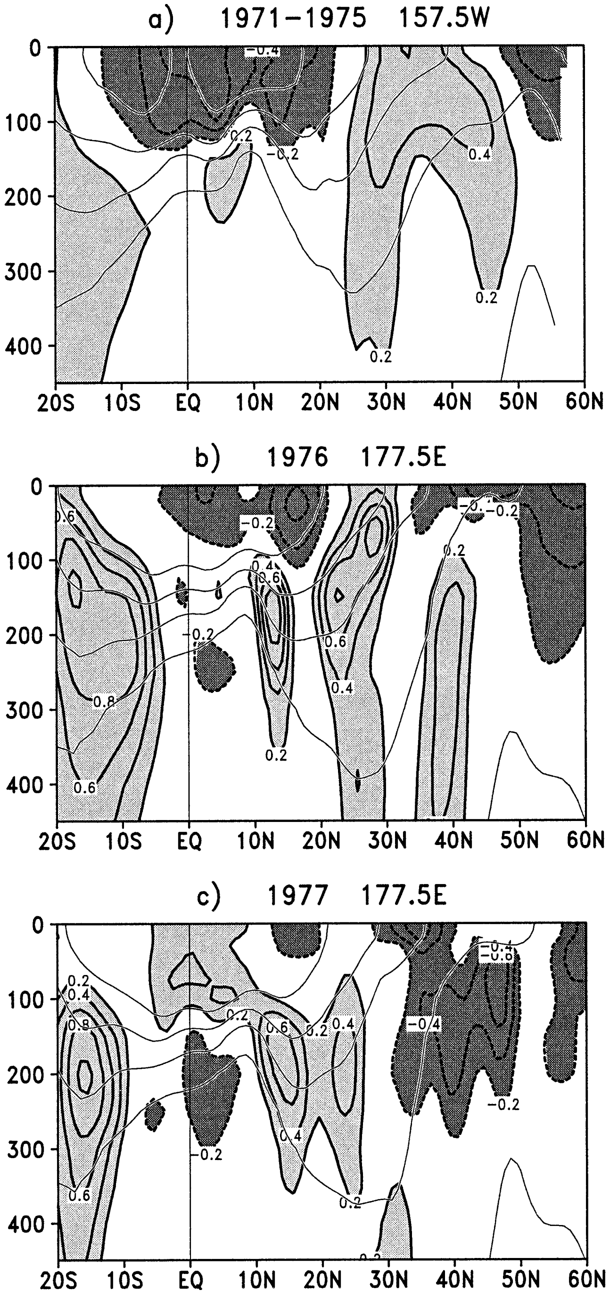

FIG. 10. Latitude–depth sections of averaged temperature anomalies along 157.5°W for (a) the years 1971–75 and along 177.5°E for the years (b) 1976 and (c) 1977. The values plotted are also zonally averaged for 5° longitude boxes whose central longitudes are described above. Contour interval is 0.2°C and zero contours are not shown. Dark and light shading indicates anomalies less than −0.2°C and greater than 0.2°C, respectively. In each panel, overlaid as thin solid lines are isopycnal contours for 23, 24, 25, 26, 27 kg m^{-3} averaged over the corresponding periods of the anomalies, with the higher density isopycnals located at the deeper levels.

experience in this study, these magnitudes and the patterns of temperature anomaly differ slightly among outputs of several trial versions of the analysis scheme and the quality control procedures.

b. Representation of El Niño anomalies

Figure 11 displays longitude–depth sections of temperature anomalies along the equator, for 1.5 yr corresponding to three El Niño episodes: (Fig. 11a) 1972–73, (Fig. 11b) 1982–83, and (Fig. 11c) 1997–98. The maps are drawn with 3-month and 1° latitude × 2° longitude averages. Temperature anomalies in the topmost panel for the 1972–73 case are averages for a season from December 1971 to February 1972, and ones for the subsequent five seasons are shown in the first column. In the same fashion, anomalies for the 1982–83 and 1997–98 cases are shown in the second and third columns, respectively.

As shown in Fig. 7, positive temperature anomalies move eastward prior to the onset of the El Niño events along the thermocline located at 100–200-m depths in the western Pacific and upper 100-m depth in the eastern Pacific. At the end of the event, these are followed by cold anomalies. Anomalies in shaded areas are regarded as significant at the 95% confidence level. From the examination of SST anomalies, which are the most reliable, it appears that the 1972–73 El Niño is weaker compared with the other two events, and the anomalies below the sea surface are weak as well.

Throughout the period of the 1997–98 event, the distribution of temperature anomalies has a strong east–west contrast along the thermocline. In the mature phase of the event, that is, from September 1997 to February 1998, temperature anomalies are more then +5°C for the upper 150 m in the eastern Pacific, and the large positive anomalies spread east of the date line. Furthermore, temperature anomalies remain positive near the sea surface during the decaying stage of the event, from March to May in 1998, while temperatures along the thermocline are 3°C colder than the climatology. These delayed changes at sea surface in the 1997–98 event are also pointed out by McPhaden (1999) using atmospheric and oceanographical data observed by TOGA–TAO buoys. In the other two events, there also appear to be characteristics similar to those of the 1997–98 events.

c. Signal-to-noise ratio

A matter of concern with regard to climate change is how much of the signal of oceanic temperature variations is detectable from the analyzed fields compared with the noise. As described in section 3, S–N ratio is directly estimated from the analysis products using the standard deviation of averaged temperature anomalies (signal) and the analysis error for averaged temperature (noise). In the following, the S–N ratio is presented for

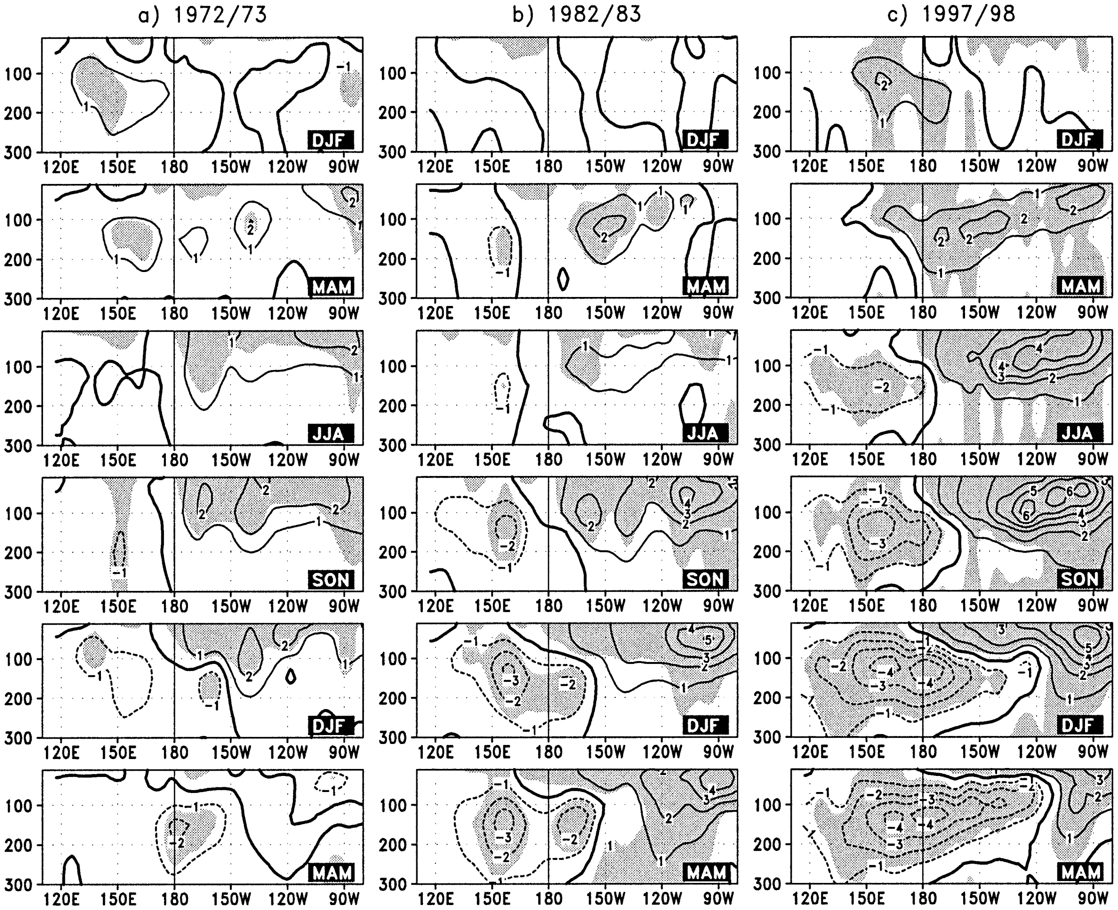

FIG. 11. Time series of temperature anomalies and analysis errors along the equator during three El Niño events: (a) 1972–73, (b) 1982–83, and (c) 1997–98. Temperature anomalies are averaged for each 3-month season, e.g., Dec–Jan–Feb (DJF). Sections of six consecutive seasons are arranged vertically for each El Niño event. Contour interval is 1°C, and shadings indicate regions where the size of the temperature anomaly exceeds the value of the analysis error multiplied by 1.65, corresponding to the 95% confidence interval.

seven areas listed in Table 2 and for five decades from 1950 to 1998. The 1990s consists of nine years.

Figure 12 shows signal (solid line) and noise (dashed–dotted line) of averaged temperatures on various temporal and spatial scales at 100-m depth in the North Pacific and in the tropical Pacific, abbreviated respectively as NP and TP in Table 2. The contours are drawn for values calculated for all combinations of five temporal scales, 1, 2, 3, 6, and 12 months, and six spatial scales, 1°, 2°, 4°, 6°, 10°, and 30°. The latitudinal extent for spatial averaging is half of the values listed above except for spatial scale 1°, because the spatial decorrelation scale of oceanic temperature is generally large in the zonal direction rather than in the meridional direction; recall the discussion about the first guess error covariances in section 3. In calculating signal and noise for a pair of temporal and spatial scales, the entire regions of NP and TP are divided into a possible number of subregions whose longitudinal extents are equal to the spatial scale. Similarly, the time series of the analyzed data in each decade are divided into sequences of monthly data whose intervals are equal to the temporal scale. The signal and noise plotted in the figure are finally given as an average of the values calculated in all the subregions and all the temporal intervals.

TABLE 2. Areas of analysis error estimates presented in Fig. 13.

Area	Label	Lat	Lon
North Pacific	NP	25°–55°N	145°E–125°W
Tropical Pacific	TP	15°S–15°N	155°E–110°W
South Pacific	SP	45°–15°S	175°E–95°W
North Atlantic	NA	25°–55°N	90°W–0°
Tropical Atlantic	TA	15°S–15°N	75°–15°W
South Atlantic	SA	45°–15°S	70°W–20°E
Tropical Indian	IN	15°S–15°N	40°–100°E

In Fig. 12, regions where the S–N ratio is less than unity are darkly shaded, while light shading indicates areas where the S–N ratio is greater than 2. In the 1970s, dark-shaded areas extend along the ordinate in the NP and TP areas. This implies that not much advantage is expected from temporal averaging for spatial scales of

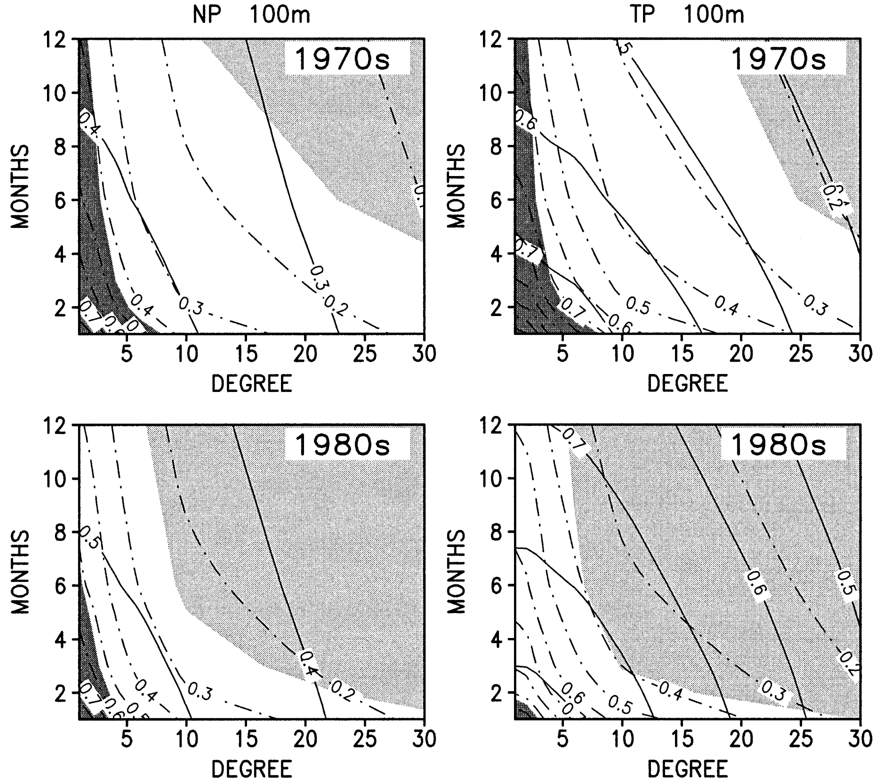

FIG. 12. Signal and noise of averaged temperatures on various spatiotemporal scales. Their values are calculated at 1°, 2°, 4°, 6°, 10°, and 30° along the abscissa and at 1, 2, 3, 6, and 12 months along the ordinate. Panels of the left-hand side and the right-hand side, respectively, correspond to regions NP and TP defined in Table 2, during (top) the 1970s and (bottom) the 1980s. In each panel, solid lines indicate standard deviations of temperature anomalies (signal) and dashed–dotted lines stand for analysis errors (noise). Dark and light shading indicates S–N ratio less than unity and greater than 2, respectively.

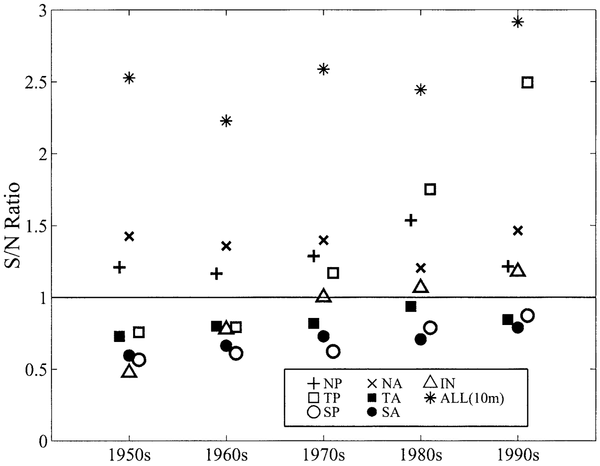

FIG. 13. The S–N ratio for 3-month and 3° lat × 6° lon box averages at 100-m depth in each decade in seven entire areas abbreviated as NP, TP, SP, NA, TA, SA, and IN (see Table 2). Refer to legend at the bottom for correspondence between symbols plotted in the figure and the ocean basins. Some symbols are shifted by ±1 yr for clearness. Asterisks indicate S–N ratio averaged over the seven basins at 10-m depth.

less than 5°. In the next decade (lower panels), the signal is larger than the noise over almost all the spatiotemporal scales, and the S–N ratio becomes larger than that of the previous decade. In the TP area, the signal is large and the noise is small in comparison with those in the 1970s. In the NP area, temperature anomalies fluctuate with large amplitudes in the 1980s rather than in the 1970s, whereas the magnitudes of analysis errors changed very little during the two decades. Because of the definition of the S–N ratio, its value is affected by interdecadal variations of the temperature anomaly. In addition, it seems that the observation density has not changed very much during the two decades in the NP area.

Next, secular changes in the S–N ratio in the above seven areas are discussed. The plotted values in Fig. 13 are S–N ratio for 100-m-depth temperatures averaged in 3° latitude × 6° longitude boxes and 3-month intervals. Additional asterisks are presented in order to show S–N ratios averaged over the seven areas at 10-m depth. Folland et al. (1993) computed the S–N ratio for GISST using SST changes of successive seasonal area-mean anomalies as the signal and differences of SST changes

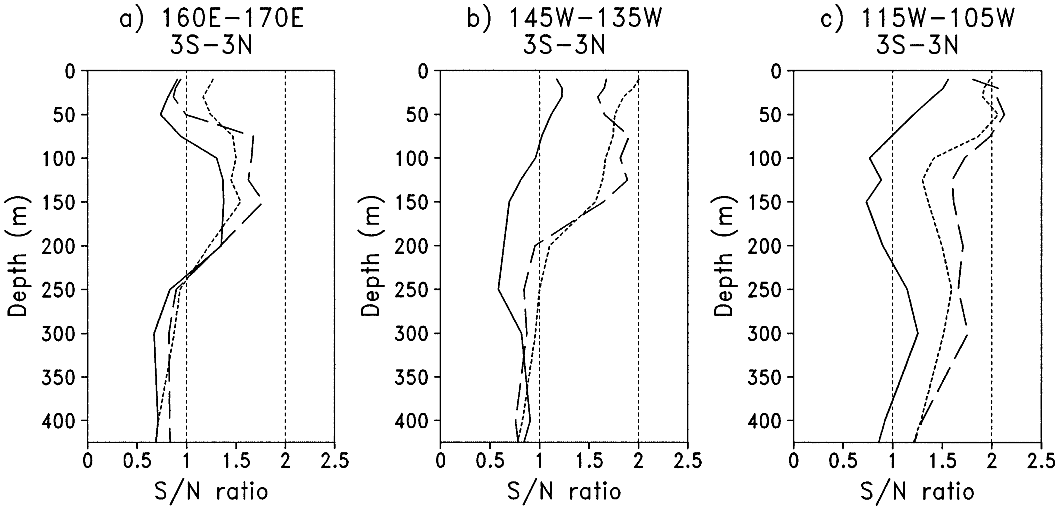

FIG. 14. Comparison of S–N ratios with a function of depth among dynamic–statistical analyses by Behringer et al. (1998) (broken) and Carton et al. (2000) (dotted), and the present statistical analysis (solid), computed in the (a) western, (b) central, and (c) eastern Pacific 6° lat × 10° lon boxes.

between GISST and in situ–satellite blended analysis by Reynolds (1988) as the noise. As shown in the figure, the S–N ratios for 10-m-depth temperature are 2–3, and are slightly smaller than S–N ratios of 3–8 for the 5° box seasonal-mean GISST. At 100-m depth, the S–N ratios are smaller by about 1 than those at 10-m depth. These facts reflect a remarkable contrast in the number of subsurface temperature observations (Fig. 2a) to the number of sea surface observations [1–2 million yr^{-1}as shown in Fig. 3 of Woodruff et al. (1987)]. A drastic improvement in the observational network over the TP area is clearly depicted; an S–N ratio of about 2.5 is seen in the 1990s, associated with the deployment of the TOGA–TAO moored arrays. In these 50 yr, the analysis error over the TP area gradually decreases by 0.3°C. Meanwhile, the standard deviation of temperature anomaly increases by 0.6°C. Such increases of the natural variability in the tropical Pacific have been found in tide gauge data (Smith 2000) and in SST and sea level pressure indices (Xue et al. 2002, manuscript submitted to *J. Climate*). Because of the definition, the S–N ratio never exceeds unity unless substantial anomalies are analyzed. Hence, data sparseness is the primary reason for the small S–N ratio. Reflecting the contrast in data distribution (Fig. 1), the S–N ratio is twice as large in the Northern Hemisphere as in the Southern Hemisphere. In the tropical Indian Ocean, the S–N ratio gradually increases and exceeds unity since the 1980s.

Finally in this section, the present analysis is compared with two dynamic–statistical analyses by Behringer et al. (1998) and Carton et al. (2000). In the latter analyses, temperature fields are obtained after observational data are optimally fitted to ocean model dynamics forced by atmospheric boundary conditions such as wind stress, heat fluxes, precipitation, and evaporation. The realization of data assimilation is rather complex. Refer to Behringer et al. (1990) and Carton et al. (2000) and the literature listed therein for further details. Figures 14a–c display S–N ratios for the seasonal mean temperatures of the three analyses with a function of depth in the western, central, and eastern Pacific (6° latitude × 10° longitude boxes) for the 1990s. The computation of S–N ratio follows Folland et al. (1993). The S–N ratios of the dynamic–statistical analyses are mostly larger than those of the present analysis. This is due to better representation of interseasonal fluctuations produced by the model dynamics and atmospheric forcing in the data assimilation. In the central and eastern Pacific, the S–N ratios of the present analysis are close to unity although the correlation coefficients of the temperature anomalies among the three analyses exceed 0.9 in the upper 150 m. The S–N ratios of the present analysis are smaller than those of TP shown in Fig. 13. However, this is not surprising because S–N ratio is not an absolute index.

d. Verification against independent data

Monthly thermal fields are verified using sea level observations by tide gauges and sea surface heights (SSHs) from the TOPEX/Poseidon satellite in this section. The monthly sea level data archive is maintained by the University of Hawaii Sea Level Center. For the purpose of verification, the satellite monthly SSH data are prepared at 1° × 1° resolution after Kurangano and Shibata (1997). They are available in the global oceans for a period from January 1993 to December 1998 except at high latitudes (>60°).

For verification against sea level and SSH, dynamic height (DH) is calculated from analyzed temperature and climatological salinity data. Salinity for a given observed temperature is determined using a mean temperature–salinity relationship; a mapping from temperature to salinity is uniquely defined at each grid point on the basis of local water mass distribution seen in the *WOA94* climatological temperature and salinity fields. In the DH calculation, a 1000-m reference level is adopted. Temperatures at depths below the 500 m are set to the *WOA94* climatology.

Before the verification, errors arising from missing salinity information are evaluated using all the *WOA94* reports with temperature and salinity observations available in the upper 500 m for the years 1950–92. These observations are interpolated to the NODC standard levels. Here, two types of DH are calculated from the observations in latitudinal bands divided every 2° between 50°S and 50°N. One is DH by mean temperature–salinity relationship and the other is DH with measured salinity observations. As a result, the correlation coefficients between the two sets of DHs exceed 0.9 at latitudes less than 40°, and the rmsd's between the two DHs are 3–6 cm in the Tropics and 5–8 cm in the extratropics. According to Busalacchi et al. (1994), the rmsd is estimated to be 2–4 cm in the equatorial Pacific between DHs from TOGA–TAO temperature and their mean temperature–salinity relationship and DHs from conductivity–temperature–depth (CTD) observations. Our rmsd's in the Tropics are slightly larger than theirs. The difference may have resulted from the databases used in the calculation and from using different estimation methods. Moreover, their values are not obtained by straightforward averaging like ours but are of an expected error (see their manuscript for detail).

In the following verification, the reference levels of analyzed DH, tide gauge data, and SSHs are adjusted to zero by subtracting their long-term averages.

Figure 15 shows time series of tide gauge (thick line) and DH (thin line) at Pago Pago in the Samoan Islands, Christmas (Kiritimati) Island, Yap Island, Naha, and San Diego. All the data plotted include seasonal cycles. The amplitudes of DH are comparable to those at tide gauge stations, Pago Pago, Christmas, and Yap in the Tropics, but smaller than those at stations in the extratropics, Naha and San Diego.

At Pago Pago, the amplitude of DH is small in the 1950s and the 1960s because of data sparseness. In later decades, it becomes large but some features seen in sea level are missing in DH. As a consequence, the correlation coefficient and rmsd between the two time series are computed as 0.39 and 6 cm, respectively, as shown in Fig. 15. It is noted that the small amplitude in the early decades may be not only due to data sparseness but also to an increase in sea level variability over the tropical Pacific as discussed in Fig. 13. At Christmas Island, located at the lowest latitude among the stations, there appears to be good correspondence between DH and sea level though the sea level data are available for only about 15 yr. At Yap Island, the DH follows well the sea level after 1970 with comparable amplitudes. However, the amplitude is small before 1970 with a remarkable contrast to the one after 1970. This is due to data sparseness below 200-m depth before 1970 (see Fig. 1). At Naha, seasonal cycles are clearly seen in both time series and a correlation coefficient results in 0.84; moreover, the interannual variations highly correlate with each other. At San Diego, large signals are seen in sea level in 1983–84, 1992–93, and 1998. During these periods, the coastally trapped waves (Gill and Clarke 1974) associated with El Niño events are observed along the coast of the North and South American continents. Similar phenomena before 1980 are documented by Enfield and Allen (1980) with sea level and temperature data. Even in DH of this study, the coastally trapped waves are represented to some extent although their amplitudes are smaller than those of sea level, as seen in the panel for San Diego. Note that the rmsd's at all stations are within the errors resulting from missing salinity. Behringer et al. (1998) report that rmsd's between the NCEP analysis and tide gauge data are reduced in the 1990s because of the completion of the TAO buoy array in this decade. A similar reduction is found between the present analysis and 29 island tide gauges located around 20°S–20°N in the Pacific; the rmsd of 5.6 cm for 1980–98 decreases to 4.7 cm for 1990–98.

Next, the DH is verified against the SSH. From a careful comparison of SSH with sea levels by Mitchum (1994), SSH errors are estimated to be less than of the order of several centimeters on timescales longer than about 10 days.

Figure 16a,b shows the geographical distribution of correlation coefficients (%) and root-mean-square differences (cm) between analyzed DH and satellite SSH for 72 months from 1993 to 1998. As pointed above concerning the results of comparisons with tide gauge data, DHs are highly correlated with SSH in lower latitudes and the correlation coefficients exceed 60% (shaded). There appear to be several regions of high correlation even in the midlatitudes of the Northern Hemisphere: the eastern parts of the North Pacific and the North Atlantic. On the other hand, the correlation coefficients are small mostly in the extratropics of the Southern Hemisphere. In Fig. 16b, areas of rmsd of less than the standard deviation of DH are shaded. These areas correspond to those with the large correlation coefficients shown in Fig. 16a. The rmsd's are 4–6 cm in the Tropics, but exceed 10 cm in the Kuroshio and Gulf Stream regions and in the extratropics of the Southern Hemisphere. In these regions, satellite SSHs have very large variability of $(10\ \mathrm{cm})^2$–$(40\ \mathrm{cm})^2$, twice that of DHs. Such variability is not represented satisfactorily by the DH fields of the present dataset.

Figure 17 displays longitude–time cross sections of the monthly DH and SSH anomalies along the equator. Here, the anomalies are relative to seasonal cycles averaged over 1993–98. As discussed above, the statistics show a good correspondence between SSH and DH in the tropical Pacific. In particular, at the equator, the mag-

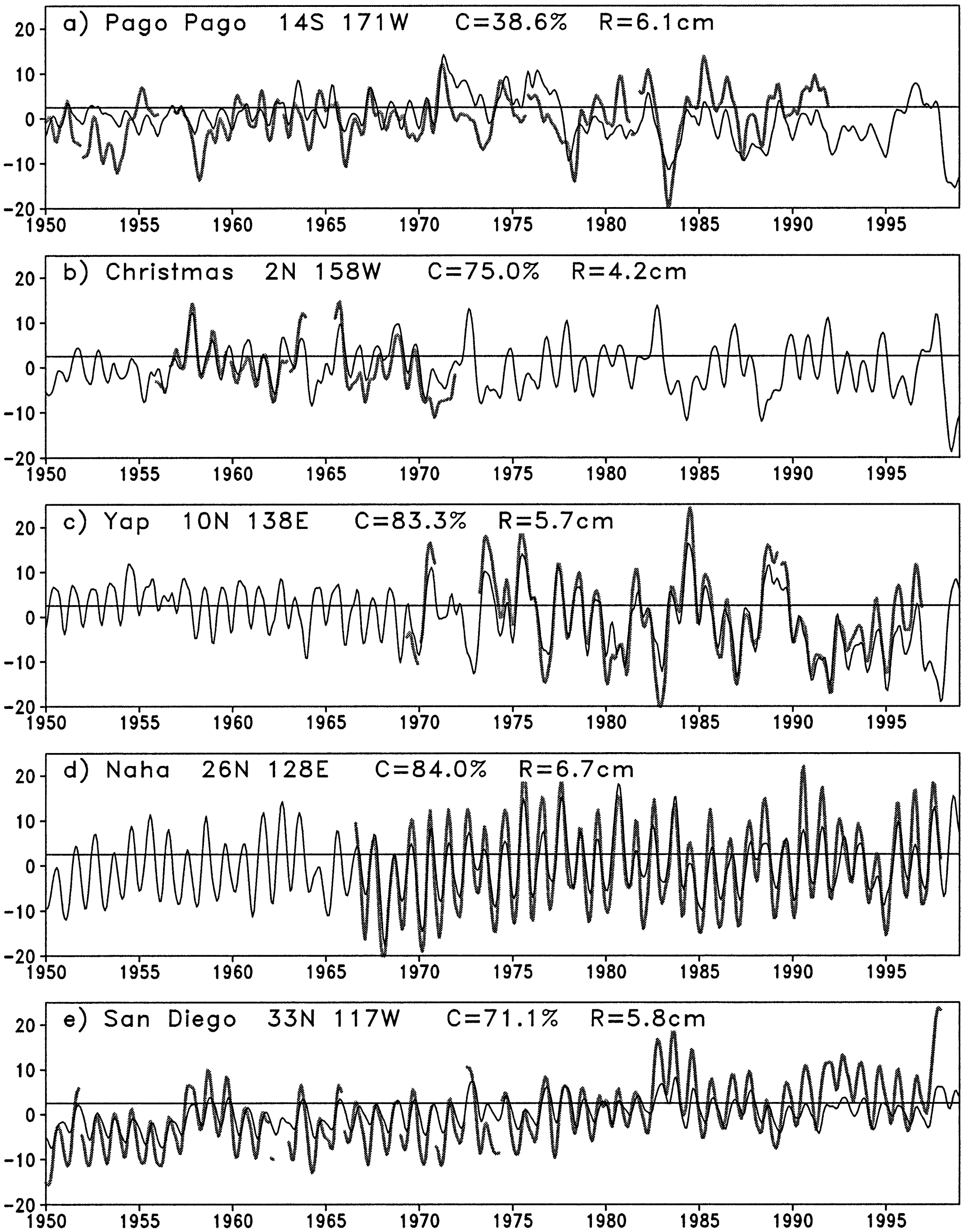

FIG. 15. Comparison between sea level by tide gauge (thick lines) and DH (thin lines) at five tide gauge stations: (a) Pago Pago (14°S, 117°W), (b) Christmas Island (2°N, 158°W), (c) Yap (10°N, 138°E), (d) Naha (26°N, 128°E), and (e) San Diego (33°N, 117°W). The values plotted are monthly averages and include seasonal cycles. Long-term averages are subtracted from the raw values. Correlation coefficient (*C*, %) and rmsd (*R*, cm) between the two time series are listed in each panel.

nitudes and temporal tendencies of the DH anomaly compare quite well with those of SSH. Examination of the S–N ratio indicates that the tropical Pacific temperatures in the 1990s are analyzed with the highest accuracy in all the decades (Fig. 13). This is due to the great contribution by the TAO buoy observations. Busalacchi et al. (1994) have reported correlations of more than 0.7 and rmsd's of less than 4 cm between 10-day gridded fields of the TAO buoy and the SSH observations. The good correspondence between the two monthly time series in the figure is consistent with their findings.

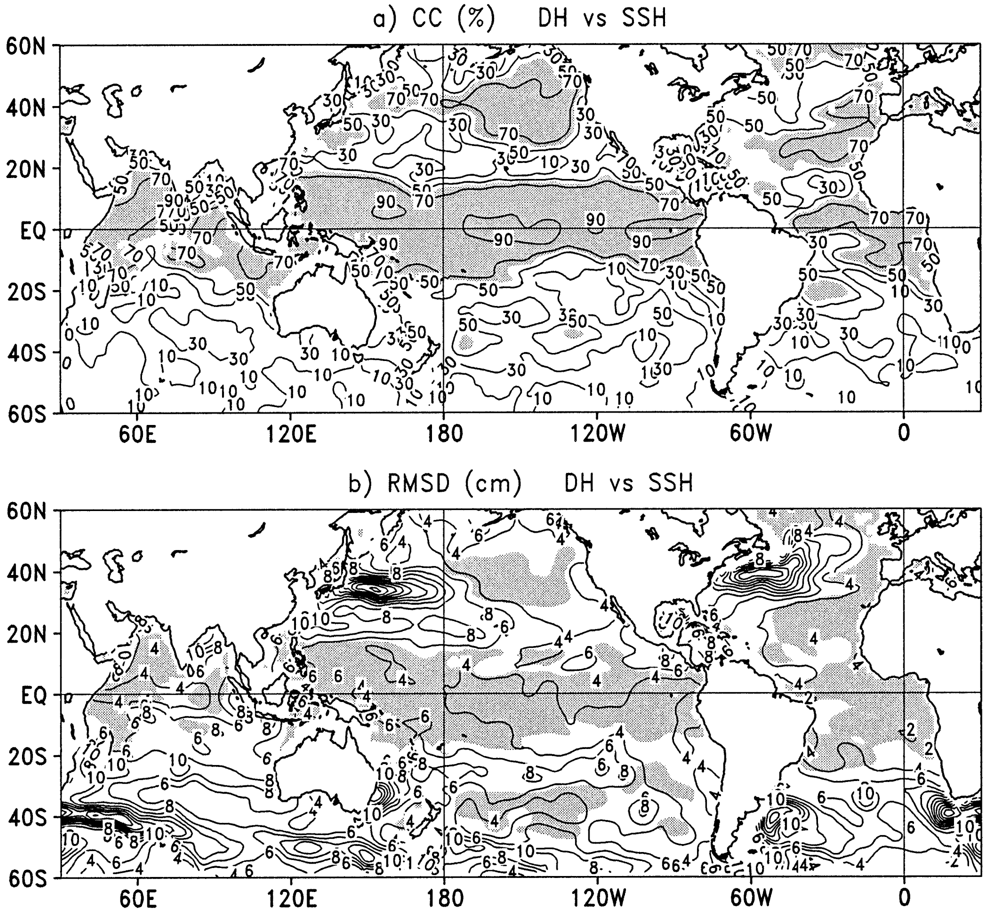

FIG. 16. Geographical distributions of (a) correlation coefficients and (b) rmsds between DH and SSH by TOPEX/Poseidon. In (a), contours of 10%, 30%, 50%, 70%, and 90% are drawn and correlation coefficients greater than 60% are shaded. In (b), the contour interval is 2 cm and shading indicates rmsds less than the standard deviations of DH. The two time series include their seasonal cycles. The period of study is 1993–98.

5. Concluding remarks

Monthly subsurface temperature analysis has been carried out during the period from 1950 to 1998 together with an estimation of analysis errors. The analyzed temperatures and the analysis errors are calculated on a 1° × 1° grid over the global oceans at 14 levels in the upper 500 m. The analysis scheme is based on a variational minimization. A conventional optimal interpolation (OI) technique is also utilized to estimate analysis errors, in which the error matrix equation is constructed with locally distributed observations around each analysis grid point, and directly solved. In the objective analysis, departures from climatology provided in the *World Ocean Atlas 1994* are optimally calculated using in situ subsurface temperature observations. All the temperature observations are subject to quality control and data selection procedures before the use in the objective analysis. In the objective analysis, sea surface temperatures (SSTs) are not analyzed, but SSTs produced by the Met Office of the United Kingdom (UKMO) are given at the sea surface, instead. In addition, the temperatures in the mixed layer are forced to remain close to the UKMO SSTs by introducing a constraint term in a variational analysis scheme. Consequently, smooth and continuous thermal fields are obtained within the mixed layer. In the present analysis, SST data are a mixture of UKMO and JMA analyses. In future studies, the data should be replaced by new UKMO SSTs developed by Parker et al. (1999).

The variational scheme is superior to the conventional OI technique because there is no data selection process involved in the temperature analysis and because it is possible to introduce prior information based on statistical or dynamical relationships to the cost function as a constraint term (e.g., Sasaki 1970). By contrast, a defect of the variational approach is that analysis errors cannot be calculated straightforwardly in most cases. Hence, in this study, the conventional OI technique is used for an estimation of the analysis error, and the vertical smoothing term in the cost function (2) is used

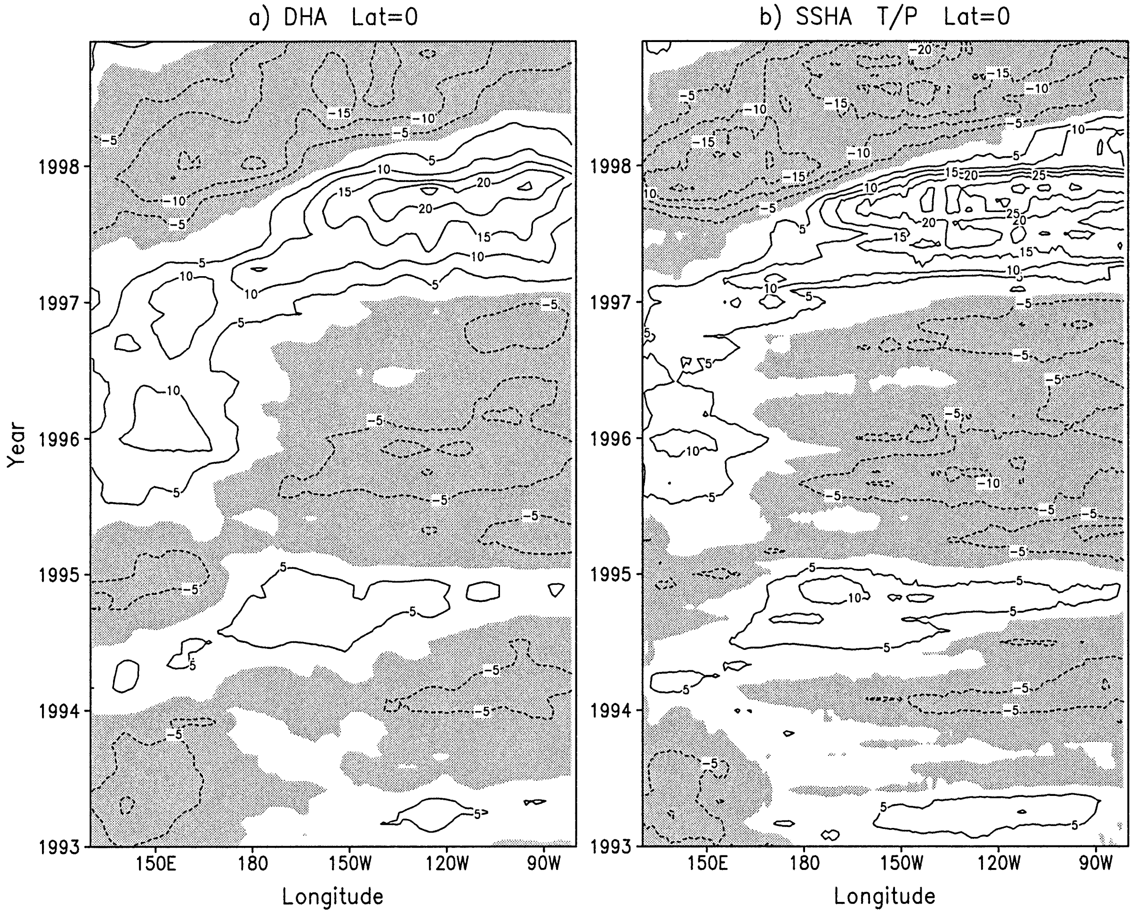

FIG. 17. Time series of (a) DH and (b) SSH anomalies along the equator. Contour interval is 5 cm and the negative values are shaded. In the both panels, the anomalies are defined as deviations from the individual averages of the period from 1993 to 1998.

in place of vertical decorrelation of the first guess error covariances. The former should be replaced by the latter, because this is more natural. This will be revised in an updated version of the analysis scheme.

By an investigation of the signal-to-noise (S–N) ratio estimated from the analysis errors, reliability of the analysis products is demonstrated on various spatiotemporal scales. Figure 12 is presented to serve as a guideline for users of the analyzed data. The investigation reveals that, during the most recent 50 yr, the S–N ratio is greater than unity but nearly constant in the Northern Hemisphere, and less than unity in the Southern Hemisphere. In the tropical Pacific, the S–N ratio gradually increases after the 1970s and attains a value of about 2.5 in the 1990s. It is realized that TOGA–TAO moored buoys greatly contribute to the effective monitoring of thermal fields in the equatorial upper oceans. In addition, an increase of the variances of the tropical Pacific subsurface temperature is influencing the large S–N ratio as well. Dynamic height anomalies estimated with analyzed temperature and climatological salinity are highly correlated in the tropical Pacific with sea level height observations from the TOPEX/Poseidon satellite for the years from 1993 to 1998. The root-mean-square differences between the two dataset are around 4–6 cm. In particular, the amplitude of the dynamic hight anomaly compares well with that of the SSH at the equator. The S–N ratio in the tropical Indian Ocean also increases in time, and exceeds unity after the 1980s. Data sparseness still remains a serious problem in the global oceans even in the 1990s, particularly, at the middle and high latitudes of the Southern Hemisphere. As discussed above, the analysis error is useful for quantitative evaluation of the data distribution.

The analysis database contains analyzed temperatures and analysis errors for about 50 yr. Using the dataset, oceanic temperatures averaged in space and time can be represented together with analysis errors on interannual and interdecadal timescales, as shown in Fig. 8. Interannual changes in the northern and tropical Pacific are represented well, for the most part, in the analysis products, though analysis errors are large locally and temporarily because of data sparseness. The dynamic heights derived from the dataset correspond well to tide gauge data as well. With the database, the thermal anomalies are examined vis-á-vis the analysis errors. It is hoped that the dataset will provide ample opportunities to examine various aspects related to interannual, decadal, and interdecadal phenomena of the global oceans in greater detail.

There is room for improvement in the quality control procedures and the objective analysis. The decorrelation scale given a priori in this study should be replaced by ones representing actual variations of ocean temperature. In order to produce persistent anomalies, the 120-day data window is adopted in the present analysis. Rather than this, it may be effective to use the analysis from the previous time step as a first guess (Reynolds and Smith 1994). Furthermore, a reconstruction technique similar to that of Smith et al. (1996) might be applicable to the subsurface temperature analyses for homogeneity.

As discussed regarding the S–N ratio above, oceanographical observations are not enough to reproduce hydrographic fields of the oceans. However, the recent proposal on a global observing array of drifting floats, Argo (Argo Science Team 1999), may possibly overcome the situation. This is more so because the Argo floats are expected to observe the temperature with an extended spatial and temporal coverage, depth range, and accuracy with additional salinity and velocity measurements. Meanwhile, data assimilation techniques have been more widely utilized in oceanographical research recently. These techniques are among the most sophisticated methodologies used for objective analysis, in which the observations are optimally fit to the ocean dynamics. The comparison with a dynamic–statistical analyses (Fig. 14) also suggests the necessity for ocean dynamics and atmospheric forcing to compensate for data sparseness and to produce more variances on interseasonal timescales. It is expected that hydrographic and kinematic fields with homogeneous quality in time and space by conventional and Argo observations in the worldwide oceans will be produced.

Acknowledgments. The bulk of this study relies on oceanic data prepared by individuals who have been engaged in observing, transmitting, archiving, and related activities. The authors wish to thank all the distributors of data used in this study: oceanic data and climatologies (NOAA/NODC), analyzed sea surface temperatures (UKMO), tide gauge data (the University of Hawaii Sea Level Center), sea surface hight data (NASA/JPL), and ocean data assimilation products (NOAA/NCEP and the University of Maryland). Many useful discussions on various aspects of oceanic data with Mr. T. Ando of JMA are thankfully acknowledged. Our appreciation is extended to Dr. K. Kumar of the Indian Institute of Tropical Meteorology for his valuable comments on the manuscript, and to Dr. T. Smith (NOAA/NESDIS/NCDC) and an anonymous reviewer for thoughtful and encouraging comments.

REFERENCES

Argo Science Team, 1999: ARGO: The global array profiling floats. *Proc. OceanObs 99 Conf.,* Saint Raphaël, France, OOPC and CLIVAR, 1–12.

Behringer, D., M. Ji, and A. Leetmaa, 1998: An improved coupled model for ENSO prediction and implications for ocean initialization. Part I: The ocean data assimilation system. *Mon. Wea. Rev.,* **126,** 1013–1021.

Bottomley, M., C. K. Folland, J. Hsiung, R. E. Newell, and D. E. Parker, 1990: *Global Ocean Surface Temperature Atlas, GOSTA plus CDROM.* HMSO, London, United Kingdom, CD-ROM.

Boyer, T. P., and S. Levitus, 1994: Quality control and processing of historical oceanographic temperature, salinity, and oxygen data. NOAA Tech. Rep. NESDIS 81, 64 pp.

Busalacchi, A. J., and J. J. O'Brien, 1981: Interannual variability of the equatorial Pacific in the 1960's. *J. Geophys. Res.,* **86,** 10 901–10 907.

——, K. Takeuchi, and J. J. O'Brien, 1983: Interannual variability of the equatorial Pacific—Revisited. *J. Geophys. Res.,* **88,** 7551–7562.

——, M. J. McPhaden, and J. Picaut, 1994: Variability in equatorial Pacific sea surface topography during the verification phase of the TOPEX/POSEIDON mission. *J. Geophys. Res.,* **99** (C12), 24 725–24 738.

Carton, J. A., G. Chepurin, and X. Cao, 2000: A simple ocean data assimilation analysis of the global upper ocean 1950–95. Part II: Results. *J. Phys. Oceanogr.,* **30,** 311–326.

Derber, J. C., and A. Rosati, 1989: A global oceanic data assimilation technique. *J. Phys. Oceanogr.,* **19,** 1333–1347.

Deser, C., M. A. Alexander, and M. S. Timlin, 1996: Upper-ocean thermal variations in the North Pacific during 1970–91. *J. Climate,* **9,** 1840–1885.

Enfield, D. B., and J. S. Allen, 1980: On the structure and dynamics of monthly mean sea level anomalies along the Pacific coast of North and South America. *J. Phys. Oceanogr.,* **10,** 557–578.

Folland, C. K., R. W. Reynolds, M. Gordon, and D. E. Parker, 1993: A study of six operational sea surface temperature analyses. *J. Climate,* **6,** 96–113.

Fu, L.-L., E. J. Christensen, C. A. Yamarone Jr., M. Lefebvre, Y. Ménard, M. Dorrer, and P. Escudier, 1994: TOPEX/POSEIDON mission overview. *J. Geophys. Res.,* **99,** 24 369–24 381.

Ghil, M., and P. Malanotte-Rizzoli, 1991: Data assimilation in meteorology and oceanography. *Advances in Geophysics,* Vol. 33. Academic Press, 141–266.

Gill, A. E., and A. J. Clarke, 1974: Wind-induced upwelling, coastal currents, and sea-level changes. *Deep-Sea Res.,* **21,** 325–345.

——, and E. M. Rasmusson, 1983: The 1982–83 climate anomaly in the equatorial Pacific. *Nature,* **306,** 229–234.

Gill, P. E., W. Murrray, and H. Wright, 1981: *Practical Optimization.* Academic Press, 401 pp.

Golub, G. H., P. C. Hansen, and D. P. O'Leary, 2000: Tikhonov regularization and total least squares. *SIAM Matrix Anal. Appl.,* **21,** 185–194.

Hanawa, K., P. Raul, R. Bailey, A. Sy, and M. Szabados, 1995: A new depth–time equation for Sippican or TSK T-7, T-6, and T-4 expendable bathythermographs (XBTs). *Deep-Sea Res.,* **42,** 1423–1451.

Hayes, S. P., L. J. Mangum, J. Picaut, A. Sumi, and K. Takeuchi, 1991: TOGA-TAO: A moored array for real-time measurements in the tropical Pacific Ocean. *Bull. Amer. Meteor. Soc.,* **72,** 339–347.

Julian, P. R., and H. J. Thiebaux, 1975: On some properties of correlation functions used in optimum interpolation schemes. *Mon. Wea. Rev.,* **103,** 605–616.

Kimoto, M., I. Yoshikawa, and M. Ishii, 1997: An ocean data assimilation system for climate monitoring. *J. Meteor. Soc. Japan,* **75,** 471–487.

Kuragano, T., and A. Shibata, 1997: Sea surface dynamic height of the Pacific Ocean derived from TOPEX/POSEIDON altimeter data: Calculation method and accuracy. *J. Oceanogr.,* **53,** 585–599.

Levitus, S., 1982: *Climatological Atlas of The World Ocean.* NOAA Prof. Paper 13. U.S. Govt. Printing Office, 173 pp.

——, and T. P. Boyer, 1994: *Temperature.* Vol. 4, *World Ocean Atlas 1994,* NOAA Atlas NESDIS 4, 117 pp.

——, T. P. Boyer, and J. Antonov, 1994a: *Interannual Variability of Upper Ocean Thermal Structure.* Vol. 5, *World Ocean Atlas 1994,* NOAA Atlas NESDIS 5, 176 pp.

——, R. Burgett, and T. P. Boyer, 1994b: *Salinity.* Vol. 3, *World Ocean Atlas 1994,* NOAA Atlas NESDIS 3, 99 pp.

McPhaden, M. J., 1995: The Tropical Atmosphere–Ocean array is completed. *Bull. Amer. Meteor. Soc.,* **76,** 739–741.

——, 1999: Genesis and evolution of the 1997–98 El Niño. *Science,* **283,** 950–954.

Miller, L., R. R. Cheney, and B. C. Douglas, 1988: Geosat altimeter observations of Kelvin waves and the 1986–87 El Niño. *Science,* **239,** 52–54.

Mitchum, G. T., 1994: Comparison of TOPEX sea surface heights and tide gauge sea levels. *J. Geophys. Res.,* **99** (C12), 24 541–24 553.

Nomura, A., 1986: An objective analysis of sea surface temperature. Numerical Prediction Division Tech. Rep. 5, Japan Meteorological Agency, 39 pp.

Parker, D. E., C. K. Folland, A. Bevan, M. N. Ward, M. Jackson, and K. Maskell, 1995: Marine surface data for analysis of climate fluctuations on interannual to century timescale. *Natural Climate Variability on Decade-to-Century Time Scales,* National Academy Press, 241–250.

——, N. A. Rayner, E. B. Horton, and C. K. Folland, 1999: Development of the Hadley Centre sea ice and sea surface temperature data set (HadISST). *Proc. Workshop on Advances in Marine Climatology—CLIMAR99,* Vancouver, BC, Canada, WMO, 194–203.

Rasmusson, E. M., and T. H. Carpenter, 1982: Variations in tropical sea surface temperature and surface wind fields associated with the Southern Oscillation/El Niño. *Mon. Wea. Rev.,* **110,** 354–384.

Reynolds, R. W., 1988: A real-time global sea surface temperature analysis. *J. Climate,* **1,** 75–86.

——, and T. M. Smith, 1994: Improved global sea surface temperature analyses using optimum interpolation. *J. Climate,* **7,** 929–948.

Sasaki, Y., 1970: Some basic formalisms in numerical variational analysis. *Mon. Wea. Rev.,* **98,** 875–883.

Schneider, N., A. J. Miller, M. A. Alexander, and C. Deser, 1999: Subduction of decadal North Pacific temperature anomalies: Observations and dynamics. *J. Phys. Oceanogr.,* **29,** 1056–1070.

Smith, N. R., 1995: An improved system for tropical ocean subsurface temperature analysis. *J. Atmos. Oceanic Technol.,* **12,** 850–870.

Smith, T. M., 2000: Tropical Pacific sea level variations (1948–98). *J. Climate,* **13,** 2757–2769.

——, R. W. Reynolds, R. E. Livezey, and D. C. Stokes, 1996: Reconstruction of historical sea surface temperatures using empirical orthogonal functions. *J. Climate,* **9,** 1403–1420.

Sprintall, J., and G. Meyers, 1991: An optimal XBT sampling network for the eastern Pacific Ocean. *J. Geophys. Res.,* **96,** 10 539–10 552.

Wang, C., and R. H. Weisberg, 2000: The 1997–98 El Niño evolution relative to previous El Niño events. *J. Climate,* **13,** 488–501.

Webster, P. J., and T. N. Palmer, 1997: The past and the future of El Niño. *Nature,* **390,** 562–564.

White, W. B., 1995: Design of a global observing system for gyre-scale upper ocean temperature variability. *Progress in Oceanography,* Vol. 36, Pergamon Press, 169–217.

Woodruff, S. D., R. J. Slutz, R. L. Jenne, and P. M. Steurer, 1987: A comprehensive ocean–atmosphere data set. *Bull. Amer. Meteor. Soc.,* **68,** 1239–1250.

Zhang, R.-H., and S. Levitus, 1996: Structure and evolution of interannual variability of the tropical Pacific upper ocean temperature. *J. Geophys. Res.,* **101,** 20 501–20 524.

——, L. M. Rothstein, and A. J. Busalacchi, 1998: Origin of upper-ocean warming and El Niño change on decadal scales in the tropical Pacific Ocean. *Nature,* **391,** 879–883.